

Long-term behaviour of a dam affected by alkali–silica reaction studied by a multi-scale model

*Original*

Long-term behaviour of a dam affected by alkali–silica reaction studied by a multi-scale model / Gallyamov, E. R.; Corrado, M.; Fauriel, J.; Molinari, J. -F.. - In: ENGINEERING STRUCTURES. - ISSN 0141-0296. - 277:(2023). [10.1016/j.engstruct.2022.115427]

*Availability:*

This version is available at: 11583/2978657 since: 2023-05-20T20:41:41Z

*Publisher:*

Elsevier

*Published*

DOI:10.1016/j.engstruct.2022.115427

*Terms of use:*

This article is made available under terms and conditions as specified in the corresponding bibliographic description in the repository

*Publisher copyright*

(Article begins on next page)



# Long-term behaviour of a dam affected by alkali-silica reaction studied by a multi-scale model

E.R. Gallyamov<sup>a,\*</sup>, M. Corrado<sup>c</sup>, J. Fauriel<sup>d</sup>, J.-F. Molinari<sup>a</sup>

<sup>a</sup>*Civil Engineering Institute, Materials Science and Engineering Institute, École Polytechnique Fédérale de Lausanne (EPFL), Station 18, CH-1015 Lausanne, Switzerland*

<sup>b</sup>*IMX LMC, Materials Science and Engineering Institute, École Polytechnique Fédérale de Lausanne (EPFL), Station 12, CH-1015 Lausanne, Switzerland*

<sup>c</sup>*Department of Structural, Geotechnical and Building Engineering, Politecnico di Torino, Corso Duca degli Abruzzi 24, 10129 Torino, Italy*

<sup>d</sup>*Alpiq Suisse SA, Ch. de Mornex 10, CP 570, 1001 Lausanne*

---

## Abstract

This paper aims to employ a 2D thermo-mechanical multi-scale ASR model for the analysis of a concrete gravity dam in Western Switzerland. Simulation results are compared to the field measurements and observations. Analysis of the results reveals no effect of temperature variation on the ASR advancement: field displacements could have been reproduced by assigning a constant temperature within an entire dam cross-section. The difference in length between the upstream and the downstream faces is identified as the main source for the upstream drift at the level of the crest. Study of the structural effects reveals ASR-related expansion anisotropy and cracks alignment being more pronounced along the upstream part and the foundation. If the former is explained by the transmission of the self-weight, the latter is attributed to the constraining effect of the underlying rock.

**Keywords:** Alkali-silica reaction, FE<sup>2</sup>, damage model, high performance computing

---

## 1. Introduction

The alkali-silica reaction (ASR) is the chemical reaction between the alkaline concrete pore solution and silica within the aggregates. It manifests itself in the form of local silica dissolution, growth of micro-cracks, their filling with the ASR products, ex-

---

\*Corresponding author

Email address: [emil.gallyamov@epfl.ch](mailto:emil.gallyamov@epfl.ch) (E.R. Gallyamov)



pansion of aggregates and paste. Micro-cracks are homogeneously distributed within the meso-structure of concrete. Mechanics of ASR depends on the stress state of concrete in two manners. First, cracks align with the direction of the prevailing load [Larive, 1997, Hilaire et al., 2017]. Second, application of a substantial compressive load ( $> 5\text{MPa}$ ) significantly reduces or fully halts ( $> 20\text{MPa}$ ) concrete expansion along this direction [Larive, 1997]. The latter constitutes so-called “stress-induced anisotropy”. Further opening and percolation of micro-cracks leads to appearance of large cracks detectable even at the macro-scale. Cracking reduces the tensile strength, the compressive strength and the elastic material properties in the order of 50 – 70%, 25 – 60% and 60 – 70% respectively [Swamy, 2003, SCD, 2017].

High relative humidity ( $> 80\%$ ) and increased temperature favour development of ASR. The most affected structures are the ones that work in a direct contact with water such as dams, bridge piers and seawalls. In this study, we will focus on the former. According to the recent study conducted in Switzerland [SCD, 2017], roughly 50% out of 154 dams are concerned by the problem. Charlwood and Sims [2017] in their comprehensive review of affected dams and hydro-projects around the world, emphasise the following typical effects of expansion:

- upstream, downstream and vertical deformation;
- map cracking on the surfaces;
- structural cracks;
- movements causing interference with gates and equipment;
- movement and leakage at horizontal lift joints due to internal expansion stresses;
- deformations affecting stability, etc.

Observations from field also suggest that ASR expansions may be restricted to certain regions in dams, such as, crest, centre and/or base or spread over the whole structure [Gunn et al., 2017]. Such ASR zonation could be due to multiple reasons, material-, structural- and environmental-dependent. On the material side, cementitious content



of a dam varies spatially, having higher values closer to the surface and along galleries. Volume fraction of aggregates (also their petrography, size and shape) may also differ between these zones. Since ASR is a process that strongly relies on the micro-structure of concrete and its chemical composition, its manifestation is expected to be different.

Possible environmental sources of non-homogeneous expansion are the variation of the relative humidity (RH) and temperature within the structure. Both fields are varying in a dam due to daily/yearly changes of surrounding temperature, fluctuation of the water level in the reservoir, variation of precipitation levels, exposure to the direct sunlight, etc. In many of the examined dams, SCD [2017] identified significant differences in concrete swelling between warm and slender upper wall areas and colder massive lower parts. Moreover, the presented data suggests certain link between the horizontal drift and the orientation of the dam axis.

Experimental data and field observations reveal high complexity of the ASR problem. This is a process that involves multiple scales and couples chemical, structural and environmental aspects. In order to understand the nature of such complex system and predict its behaviour, numerical modelling is an indispensable tool. A comprehensive review of modelling approaches classified by physical scales was done by Esposito and Hendriks [2019]. Models, aimed to describe the physics at the finest scales (level of concrete micro-structure), include most of the relevant physics, such as transport of chemical components and humidity [Alnaggar et al., 2017, Multon and Sellier, 2016, Puatatsananon and Saouma, 2013, Bangert et al., 2004], temperature effect [Ulm et al., 2000], pressure build-up due to the products formation [Multon and Sellier, 2016], micro-cracks opening [Dunant and Scrivener, 2010, Cuba Ramos et al., 2018, Miura et al., 2021] and their interplay with the stress state [Dunant and Scrivener, 2012b].

On the structural level, the macroscopic numerical models resolve spatial variations of the stress, temperature and humidity fields, the 3D shape of a structure, and different boundary conditions. The above-mentioned micro-scale physics is included into these models either in a phenomenological way [Gocevski and Yildiz, 2017, Comi et al., 2009, Menouillard et al., 2011] or derived by homogenisation principles [Bangert et al., 2004, Iskhakov et al., 2019]. The ASR-induced damage is typically assumed to



be isotropic. In some models, anisotropic swelling is simulated by introducing phenomenological anisotropy factors [Multon and Toutlemonde, 2006, Comi et al., 2009]. These factors are later calibrated by laboratory experiments or field measurements. The before-mentioned approaches in general provide fair predictions of material and structural behaviour and are efficient to use.

Having all the merits, these models cannot, however, directly describe the microscopical state of the material. The typical output could be scalar parameters of damage and reaction extent, anisotropy level and quantities of reactants. This data is scarce for researchers who want to study an interplay between microscopic expansion and macroscopic structural behaviour. Resolving massive hydro-structures at the level of aggregates is not yet possible, despite continuous advancement of high-performance computing.

To overcome this obstacle, various multi-scale methods could be efficiently employed. In this paper, attention is restricted to a specific method called multi-scale computational homogenisation [Kouznetsova et al., 2001, Feyel and Chaboche, 2000, Miehe et al., 1999, Renard, 1987]. Its idea is to have two boundary value problems (BVP), one at each scale, and solve them simultaneously, in a fully nested manner. This procedure allows to evaluate the macroscopic influence of micro-structural parameters in an explicit manner. Such a model applied to the ASR problem was recently introduced by the authors [Gallyamov et al., 2020]. The fine scale model consists of a representative volume element (RVE) comprising aggregates of various sizes, pockets of the ASR product distributed within aggregates, all embedded in cement paste. To simulate ASR, pockets of the ASR product are expanding and imposing internal pressure on the micro-structure, which leads to the development of cracks and overall expansion of RVEs. Application of this fully coupled two-scale computational homogenisation approach allows the detailed study of the damage evolution at the meso-scale and of the deformations development at the structural level. The results obtained from this study provide physical insights into the long-term behaviour of ASR-affected dams.

The objective of the present paper is the analysis of the structural effects of ASR within a dam by solving the concrete deterioration problem at the meso-scale level. We



are aiming to understand the interplay between the macroscopic state (stresses, deformations and their anisotropy) and the mesoscopic state of concrete (amount of cracks, their percolation, opening and orientation). Moreover, we study the role of the seasonal temperature variation across the dam in the advancement of ASR. We compare the model sensitivity to the temperature fluctuations in the field and the laboratory conditions. Such comparison allows to identify possible reasons for the gap between these two environments. We employ a 2D thermo-mechanical multi-scale model of a dam with the concrete micro-structure resolved numerically. A unique set of continuous 67 years-long field measurements from an ASR-affected gravity dam in Switzerland allows for an improved model calibration and quantitative interpretation of the results.

The rest of the paper is organised as follows. First, the proposed multi-scale approach is briefly summarised in Section 2. Further, Section 3 describes the problem at hand, giving details on the geometries of the macro-scale model and RVEs, and applied boundary conditions for mechanical and heat transfer models. Results of the simulation and their interpretation are presented in Section 4. Finally, concluding remarks and further outlook are given.

## **2. Numerical modelling**

The considered problem has large differences in length scales. The first ASR products are formed as thin layers between mineral grains. They have thickness from nanometer scale up to few micrometers [Leemann and Münch, 2019]. The formation of these layers induces cracking of aggregates, which have sizes ranging from millimetres up to few centimetres. Further reaction evolution forces cracks to grow, merge and spread also into the cement paste. On the structural scale, a typical dam could measure up to few hundred of meters in height and length. Thus, the length scale of the problem at hand ranges from few nanometers up to hundreds of meters. In order to avoid full resolution of such immense system, a computational homogenisation method, also called  $FE^2$ , is applied. The idea behind it is to split a macro-scale problem into large elements and represent each element by a separate boundary value problem called representative volume element. RVEs have structure typical to the scale of interest and



have to be resolved to a sufficiently fine level of details to be able to capture the relevant physics. An RVE could also be seen as a constitutive behaviour of macro-scale elements embedded in a separate model. The whole computational homogenisation framework relies on the separation of scales principle: the characteristic length scale of a fine scale structure,  $l_\mu$ , must be smaller than the size of considered RVE,  $l_m$ , which, in its turn, has to be significantly smaller than the characteristic fluctuation length of the macroscopic deformation field,  $l_M$ .

$$l_\mu < l_m \ll l_M, \quad (1)$$

The difference in sizes between the macro-scale region and its fine-scale representation could be as large as necessary under conditions that Eq. (1) is fulfilled. Note that in this work, the fine-scale of the  $\text{FE}^2$  problem is the meso-scale of concrete.

In the  $\text{FE}^2$  scope, the macro-scale deformation gradient  $\mathbf{F}_M$  at each macroscopic integration point is assigned to each RVE as a boundary condition. Additionally to  $\mathbf{F}_M$ , any other relevant macroscopic field could be passed to the fine-scale, for example the macroscopic temperature  $T_M$ , necessary for the reaction advancement. Solution of the fine-scale problem results, after application of an averaging procedure, in a macroscopic stress tensor  $\boldsymbol{\sigma}_M$ . In such way, RVEs are employed to establish a stress-strain relationship available at the macro-scale. Furthermore, non-linear problems typically require iterative procedure to arrive to an equilibrated solution.  $\text{FE}^2$  approach also has an iterative loop at the macro-scale, when the fine-scale solution is recomputed for the changing macroscopic displacement field. For a classical iterative approach, such as Newton-Raphson, the consistent tangent stiffness at the macroscopic integration point  $\mathbb{C}_M$  is required for solution of the displacement field. This stiffness is computed per RVE via homogenisation and later assembled in a global macroscopic tensor. Convergence at the macro-scale is verified by controlling the balance between the external and the internal forces. The first-order  $\text{FE}^2$  scheme is depicted in Fig. 1. In the following, the subscripts  $M$  and  $m$  will be used to denote physical quantities at the macro- and meso-scales, respectively.



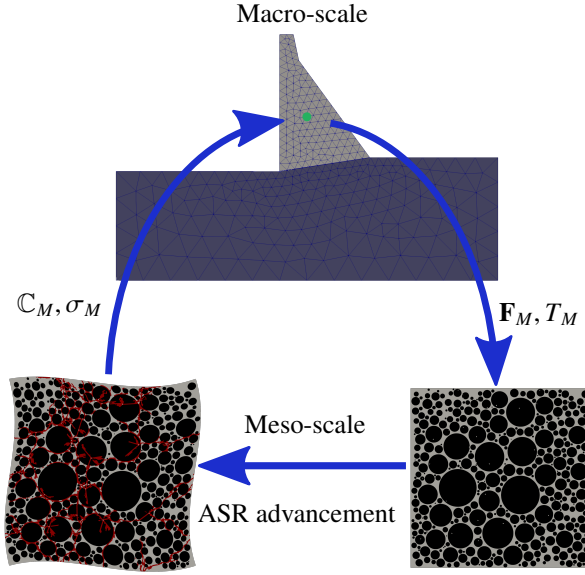


Figure 1: Schematic illustration of the computational homogenisation scheme for the ASR simulation of a dam. The macro-scale comprises the dam itself and the rock mass below.

The presented model is thermo-mechanical at the macroscopic scale and purely mechanical at the RVE level. However, the effect of temperature enters RVEs through the ASR-product expansion law. The moisture diffusion process, which governs the evolution of the chemical reaction, is not taken into account, and it is assumed that the dam is fully saturated. Previous study by Comi et al. [2012] showed that, for particular environmental conditions and water-reservoir level, this assumption is valid and only a thin layer of concrete in contact with air (about 40 cm) is dry.

Thermo-elastic expansion is ignored both at the macro- and meso-scales. At the macroscopic scale, this is done mainly to separate displacements of a dam due to yearly temperature fluctuations from continuous ASR-caused drift. For more details on this subject, readers can refer to the comprehensive study of the dam deformations due to the thermo-elastic expansion by Aniskin and Shaytanov [2020]. At the meso-scale, assuming that the thermo-elastic properties of damaged material are similar to the undamaged ones, the thermo-elastic expansion should not cause any difference in results due to the homogeneous temperature across an entire RVE. This is however a



simplification that should be addressed in future work.

In the remainder of this section, we briefly discuss the main principles of the FE<sup>2</sup> approach, and the formulation and solution of the macro- and meso-scale models. Few words are written about the material behaviour. Finally, the section is concluded by the introduction of the heat transfer model. For full details on the computational homogenisation technique applied to the ASR problem and its validation against a full-scale model, readers are referred to the study of Gallyamov et al. [2020].

### 2.1. Multi-scale model

Considering the slow rate of ASR, the problem is considered quasi-static. Solution to the BVP at both scales is obtained by applying the principle of virtual work:

$$\delta W = \int_{\Omega} \boldsymbol{\sigma} : \delta \boldsymbol{\varepsilon} d\Omega - \int_{\Omega} \mathbf{b} \cdot \delta \mathbf{u} d\Omega - \int_{\Gamma_t} \mathbf{t} \cdot \delta \mathbf{u} d\Gamma = 0, \quad (2)$$

where  $\Omega$  denotes the domain of the BVP,  $\Gamma$  is its external boundary, which is decomposed into non-overlapping Neumann  $\Gamma_t$  and Dirichlet boundaries  $\Gamma_u$ ,  $\delta W$ ,  $\mathbf{b}$  and  $\mathbf{t}$  denote the virtual work, body forces and tractions, and  $\delta \boldsymbol{\varepsilon}$  and  $\delta \mathbf{u}$  the virtual strains and virtual displacements. Eq. (2) is discretized and solved by the finite element method (FEM).

When applying Eq. (2) at the macroscopic problem, stress tensor  $\boldsymbol{\sigma}_M$  is obtained directly from the RVE computations. First, the stress distribution inside the RVE is obtained from the solution of the meso-scale boundary value problem (BVP). Then, for the macro-scale, the average stress response of the RVE is determined by the spatial averaging of the meso-scale stresses inside the RVE:

$$\boldsymbol{\sigma}_M = \frac{1}{\Omega_m} \int_{\Omega_m} \boldsymbol{\sigma}_m d\Omega_m. \quad (3)$$

This derives from the *Hill-Mandel* macro-homogeneity condition [Hill, 1963] which, among others, is fulfilled by application of periodic fluctuations boundary conditions, as was shown by Suquet [1987]. The latter were chosen due to better estimates for the effective stiffness [Coenen et al., 2012].



Effective macroscopic tangent stiffness tensor is derived through the effective stress-strain relation

$$\boldsymbol{\sigma}_M = \mathbb{C}_M \boldsymbol{\varepsilon}_M. \quad (4)$$

In 2D, the symmetric fourth-order tensor  $\mathbb{C}_M$  is determined by three virtual loading tests, linearly independent from each other. Each of them provides one column for the symmetric second-order tensors  $\boldsymbol{\sigma}_M$  and  $\boldsymbol{\varepsilon}_M$ . Due to the difference in behaviour of cracked material in tension and in compression, the direction of the virtual loading tests is chosen based on the sign of the hydrostatic component of the RVE's stress state.

The boundary conditions for RVEs are prescribed in terms of the macroscopic deformation gradient, which is not known *a priori* and depends on the balance between macro- and meso-scales. An iterative procedure is employed to get the solution. Initial macroscopic deformation is imposed and a series of solution steps are performed until reaching convergence. The latter is based on the balance between external and internal forces at the macro-scale. The algorithm for the current multi-scale implementation is detailed in Algorithm 1.



---

**Algorithm 1:** Multi-scale algorithm for ASR-affected concrete.

---

```
for every integration point at the macro-scale do
    Generate an RVE;
for every time step  $i$  do
    Apply thermo-mechanical boundary conditions at the macro-scale ;
    Solve the macroscopic heat transfer problem;
    Pass temperature information from the macro- to the meso-scale;
    for every RVE do
        Based on the temperature, compute ASR products expansion value;
        Impose expansion at the ASR sites;
    while solution is not converged do
        Solve the mechanical macro-scale problem;
        for every RVE do
            Collect deformation gradient from the macro-scale;
            Apply it as boundary conditions at the meso-scale;
            while finite elements are damaged do
                Solve the meso-scale problems;
                Reduce material properties of the damaged elements (SLA);
            Homogenise stress;
            Determine hydrostatic component of the homogenised stress;
            Homogenise the RVE stiffness;
        Assemble global stiffness matrix;
        Assemble macro-scale internal force;
        Check for convergence;
    Output results;
```

---

## 2.2. Materials behaviour

An RVE represents a concrete structure at the meso-scale. It comprises three mutually exclusive solid phases: the mortar, which includes the cement paste and the sand,



the aggregates, and the ASR-product sites. The ASR reaction manifests itself in form of ASR sites expansion, which applies internal pressure on the meso-scale structure. In this study we assume that the total volume increase of the ASR product is proportional to the isotropic eigenstrain  $\boldsymbol{\varepsilon}_{m,eig}$  increase and we impose the latter at each ASR site. The eigenstrain is linked to the elastic strain  $\boldsymbol{\varepsilon}_{m,el}$  and the displacement field via the following equations:

$$\boldsymbol{\varepsilon}_m = \boldsymbol{\varepsilon}_{m,el} + \boldsymbol{\varepsilon}_{m,eig}, \quad (5)$$

$$\boldsymbol{\varepsilon}_m = \frac{1}{2} (\nabla \mathbf{u}_m + \nabla \mathbf{u}_m^T), \quad (6)$$

where  $\boldsymbol{\varepsilon}_m$  is the infinitesimal strain tensor and  $\nabla \mathbf{u}_m$  is the deformation gradient at the meso-scale. We use the ASR expansion law based on a first-order kinetics in isothermal conditions:

$$\boldsymbol{\varepsilon}_{m,eig}(t, T) = \boldsymbol{\varepsilon}(\infty) \frac{1 - \exp[-t/\tau_{ch}(T)]}{1 + \exp[-t/\tau_{ch}(T) + \tau_{lat}(T)/\tau_{ch}(T)]} \mathbb{I}, \quad (7)$$

$$\tau_{ch}(T) = \tau_{ch}(T_0) \exp[U_C(1/T - 1/T_0)], \quad (8)$$

$$\tau_{lat}(T) = \tau_{lat}(T_0) \exp[U_L(1/T - 1/T_0)], \quad (9)$$

where  $t$  and  $T$  are the current time and temperature, and  $\mathbb{I}$  is the identity matrix,  $\boldsymbol{\varepsilon}(\infty)$  is the asymptotic volumetric expansion strain in the stress-free experiment,  $T_0$  is the reference temperature,  $U_C$  and  $U_L$  are the activation energy constants [Ulm et al., 2000, Larive, 1997]. The latency time  $\tau_{lat}(T_0)$ , the characteristic time  $\tau_{ch}(T_0)$  and the asymptotic value of the local strain  $\boldsymbol{\varepsilon}(\infty)$  are the calibration parameters of the model. The presence of the exponential functions introduces Arrhenius-like dependence of the expansion rate on the temperature.

Leemann and co-workers [Leemann et al., 2016, Leemann and Münch, 2019] have shown that the typical size of an early-phase ASR inclusion is few nanometers. In the current numerical study, the size of the finite elements in the RVEs is 0.5 mm. The expansion  $\boldsymbol{\varepsilon}_{m,eig}$ , applied at a single element, should be seen as an average expansion of an aggregate area comprising one or multiple pockets of the ASR product. In this way,



mechanical processes taking place at the nano-scale are accounted in a homogenised manner.

In this ASR meso-scale model the aggregates and the mortar are assumed to be quasi-brittle materials and the ASR product is modelled as linear elastic. Its expansion causes high stresses in the surrounding material. It is assumed that the material fails locally always under tension with subsequent linear softening. The constitutive law is depicted in Fig. 2a.

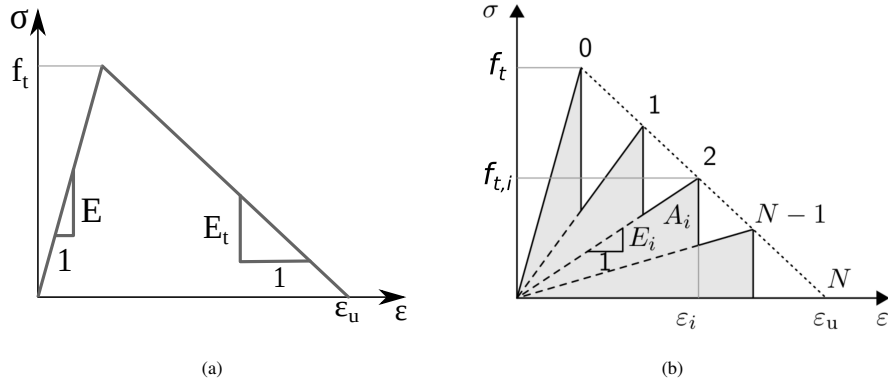


Figure 2: (a) Bi-linear law with an initial elastic loading phase and subsequent linear strain-softening. (b) Stress-strain curves obtained with the SLA.

Cracking in concrete due to ASR is modelled by the fixed crack model with stiffness recovery upon crack closure [Rots and Blaauwendraad, 1989]. The idea behind is to model continuum as an elastic-brittle orthotropic material with its elastic properties degraded in a single direction that is chosen in the first damaging event (see Fig. 3). Details on modeling orthotropic behaviour could be found in a classical textbook by Bower [2009].

Fracture energy invariance is achieved by means of the crack band model [Bažant and Oh, 1983]. Micro-cracks are smeared over the fracture process zone of width  $w_c$ , taken equal to the average element size. The fracture energy  $G_c$  normalised by the crack band width  $w_c$  equals

$$\frac{G_c}{w_c} = \int_0^\infty \sigma d\varepsilon^f = \frac{1}{2} f_t^2 \left( \frac{1}{E} - \frac{1}{E_t} \right), \quad (10)$$



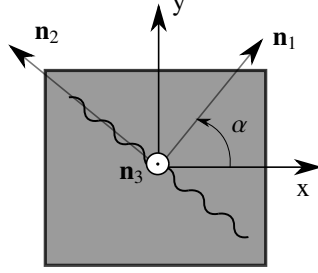


Figure 3: Illustration of an element with a fixed crack.

where  $\varepsilon^f$  is the fracturing strain,  $E$  is the initial material stiffness in the direction perpendicular to the crack,  $E_t$  is the tangent to the tensile stress-strain softening curve (see Fig. 2a). In all meso-scale simulations, the crack band width,  $w_c$ , is taken equal to the element size of 0.5 mm. The crack band model is effective in preserving the fracture energy of a single-crack geometry. However, it is less precise when problems with multiple intersecting cracks are modelled.

For the undamaged material, all the elastic properties equal the initial isotropic values:

$$E_k = E, \quad \nu_{kl} = \nu, \quad \mu_{kl} = \mu, \quad (11)$$

where  $E_k$  is the Young's modulus in the direction of the basis vector  $\mathbf{n}_k$ ,  $\nu_{kl}$  and  $\mu_{kl}$  are the Poisson's ratio and the shear modulus between directions  $\mathbf{n}_k$  and  $\mathbf{n}_l$ . If a crack starts growing along the plane  $\mathbf{n}_2\mathbf{n}_3$ , as shown in Fig. 3, the material properties for the perpendicular direction  $\mathbf{n}_1$  are reduced according to:

$$E_1 = E(1 - d), \quad \nu_{12} = \nu_{13} = \nu(1 - d), \quad \mu_{12} = \mu_{13} = \mu(1 - d). \quad (12)$$

Material properties in the undamaged directions stay unchanged and equal to the initial isotropic value.

An indication for the stiffness recovery upon crack closure is the strain perpendicular to the crack becoming negative. This activates the full recovery of the Young's modulus and Poisson's ratio, while keeping the shear modulus low under assumption



of a friction-less crack:

$$E_k = E, \quad \nu_{kl} = \nu, \quad \mu_{kl} = \mu(1 - d).$$

In order to avoid convergence issues, failure in aggregates and mortar are computed by means of the modified sequentially linear analysis (SLA, Rots and Invernizzi [2004], Rots [2001], DeJong et al. [2008]). In its scope, incremental solution of the strain-softening behaviour of an element is substituted by a sequence of linear elastic steps with gradually reduced stiffness. In such a way, there is no need to compute tangent stiffness, and the convergence check at the meso-scale becomes also unnecessary. The essence of this method is illustrated in Fig. 2b. In every step, the integration point with the highest stress is detected and the loading is down-scaled to the exact value at which this integration point (IP) arrives at the failure envelope. Then, its stiffness and strength are reduced according to the current damage value  $d_i$ , which is defined as

$$d_i = 1 - \frac{1}{a^i}, \quad (13)$$

where the empirical reduction constant  $a$  is brought to the power  $i$  which is the number of the reduction step. In the following simulations,  $a = 2$  and  $i_{max} = 10$ . After damaging event, loading is further increased and the next most stressed IP is identified. Like this, the final loading is reached in number of intermediate steps. Application of the classical SLA to an  $FE^2$  model is complicated due to discontinuous in time boundary conditions applied at the RVE's corner nodes. In order to overcome this complications, the classical SLA scheme was altered by two modifications. First, the loading increase was fixed to a constant sufficiently small value which is still reasonable from the computational time perspective. As in our model the loading is proportional to the time step, the latter was chosen to be 15 days. By the second modification, we permitted multiple highly stressed IPs to be damaged within one iteration. The latter is done to speed up the computations. The number of simultaneously damaged IPs is controlled



by the threshold parameter  $\zeta$ . An IP will be damaged if the following equation holds:

$$\sigma \geq (1 - \zeta)\sigma_{max}, \quad (14)$$

$$\sigma_{max} \geq f_{t,i}, \quad (15)$$

where  $\sigma$  is the principal stress at this IP,  $f_{t,i}$  is its tensile strength and  $\sigma_{max}$  is the maximum principal stress. This allows multiple IPs, having stress slightly below the maximum, to be equally damaged. In the current study,  $\zeta$  was taken equal to 0.01. The tensile strength is reduced as

$$f_{t,i} = \varepsilon_u E_i \frac{E_t}{E_i + E_t} \quad (16)$$

with the softening slope

$$E_t = \frac{f_t}{\varepsilon_u - (f_t/E)}. \quad (17)$$

### 2.3. Heat transfer model

Assuming no mass transfer or radiation, the energy conservation equation for non-uniform isotropic medium is written as

$$\rho c_p \frac{\partial T}{\partial t} - \nabla \cdot (k \nabla T) = b, \quad (18)$$

with  $T$  being the scalar temperature field,  $c_p$  the specific heat capacity,  $\rho$  the material density,  $k$  the thermal conductivity, and  $b$  the volumetric heat source. The first term of the equation above is responsible for the heat accumulation by a volume, the second for its diffusion to a colder area, and the right-hand side for the heat generation.

Similar to the mechanical part, the heat transfer problem is discretized by the finite element method (FEM). Accounting for the dynamical nature of heat transfer problem, Eq. (18) is solved implicitly, which makes the solution unconditionally stable and does not limit the time step size.

In the current study, we adopt a one-way coupling scheme. The heat transfer model affects the mechanical one by altering the ASR-product growth rate (Eq. (7)), while the reverse influence of the stress and damage states on the thermal parameters in Eq. (18)



is omitted.

At each time step, first, the heat transfer model is solved for the given boundary conditions. Then, the updated temperature field is passed to the macro-scale model, which in its turn transfers local temperatures to the corresponding RVEs. After that, the mechanical multi-scale problem is solved iteratively.

Thermal properties of concrete are specified in Table 1. Due to the unknown geological situation and a wide range of possible thermal rock properties [Robertson, 1988], the latter were taken equal to the concrete ones.

Thermal conductivity $K$ , W/(m K)	1
Specific heat capacity $C$ , kJ/(kg K)	1

Table 1: Thermal properties of concrete and rock.

### 3. Simulations

For the simulation of a dam, the parameters of the ASR-expansion law had to be previously calibrated. Such calibration was done on the set of laboratory experiments by Multon and Toutlemonde [2006]. These authors studied the ASR-anisotropy due to macroscopic loading by letting cylindrical specimens of concrete with ASR expand either freely or under longitudinal and radial loads. Macroscopic ASR-related deformations were derived by subtracting deformations due to elasticity, shrinkage and creep. The calibration of the model was the object of a preceding paper [Gallyamov et al., 2020] and, therefore, only a short overview of the calibration is herein reported, followed by the formulation of the macroscopic thermo-mechanical problem and its boundary conditions.

#### 3.1. RVEs calibration

An RVE comprises a two-dimensional square body of size  $70 \times 70 \text{ mm}^2$  composed of circular aggregates with ASR-product sites, embedded in mortar. The Fuller curve is used as a grading curve for the generation of aggregates, whose diameters lay in the range 1–16 mm. The aggregate packing density reaches 70%. In real dam concrete,



maximum size of aggregates could go up to 160 mm, which makes the chosen size range under-representative. Increasing the maximum aggregates size would cause increase in the RVE size which is avoided for the computational capacity reason. The aggregate size distribution is, however, a model parameter which might affect the final results.

The geometrical model is later discretized into a finite-element mesh of linear triangular elements with a uniform element size  $h = 0.5$  mm. Resulting RVE with boundary conditions for the calibration tests is visualised in Fig. 4.

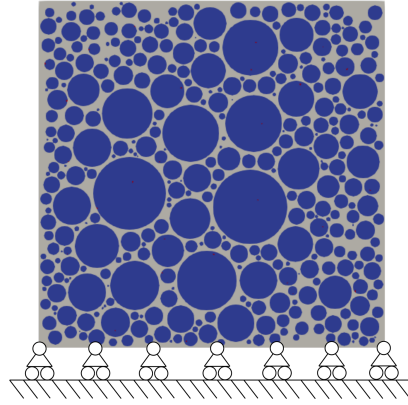


Figure 4: Concrete micro-structure and boundary conditions for the calibration tests.

The elastic and fracture properties of concrete and ASR-product are summarised in Table 2. Shear modulus  $\mu$  is computed as  $\mu = E/[2(1 + \nu)]$ . Tensile strength  $f_t$  is distributed within aggregates and paste according to Weibull distribution. The calibrated parameters of the ASR expansion law are listed in Table 3. The model is calibrated based on the free ASR-expansion experiment, where only the internal load coming from the expanding ASR-sites is present. Same parameters were used to simulate the compressed ASR-expansion experiment with a uniaxial pressure of 10 MPa. Both simulations were conducted under the constant temperature of 38°C.



	$E$ [GPa]	$\mu$ [GPa]	$\nu$ [-]	$G_c$ [J/m <sup>2</sup> ]	$f_t$ [MPa]
Aggregates	59 <sup>1</sup>	22.6	0.3 <sup>1</sup>	160 <sup>2</sup>	10 <sup>2</sup>
Mortar	12 <sup>1</sup>	4.6	0.3 <sup>1</sup>	60 <sup>3</sup>	3 <sup>1</sup>
ASR product	11 <sup>4</sup>	4.7	0.18 <sup>4</sup>	-	-

Table 2: Material properties.

Ratio of the ASR sites area to the aggregates area	0.1 %
Asymptotic strain $\epsilon(\infty)$	6.5 %
Latency time $\tau_{lat}$	30 days
Characteristic time $\tau_{ch}$	60 days
Reference temperature $T_0$	38°C
Energy constant $U_C$	5400 K
Energy constant $U_L$	9700 K

Table 3: Calibrated parameters and constants of the ASR-expansion law presented by Gallyamov et al. [2020].

Results of the calibration, performed by Gallyamov et al. [2020], both for free-expansion and uniaxially loaded cases are plotted in Fig. 5. Calibration comprised a Monte Carlo simulation with 200 realisations of concrete micro-structure. In both cases expansion curves have asymptotic shape with saturation time around 200 days. While both free-expansion curves and the longitudinal expansion of the loaded specimen match the experiment quite well, its latitudinal counterpart is exceeding the experimental average value by roughly 25%. This could mainly be due to the comparison of a 2D simulation with a 3D experiment. A 2D model would have less space to accommodate cracks, thus final expansion is supposed to be larger.

The crack opening maps of the free and the loaded concrete specimens are shown in Fig. 6. Here, openings of damaged elements are plotted. The darkest shade corresponds

<sup>1</sup>Taken from [Dunant and Scrivener, 2012a].

<sup>2</sup>Taken from [Ben Haha, 2006].

<sup>3</sup>Taken from [Xu and Zhu, 2009].

<sup>4</sup>Taken from [Leemann and Lura, 2013].



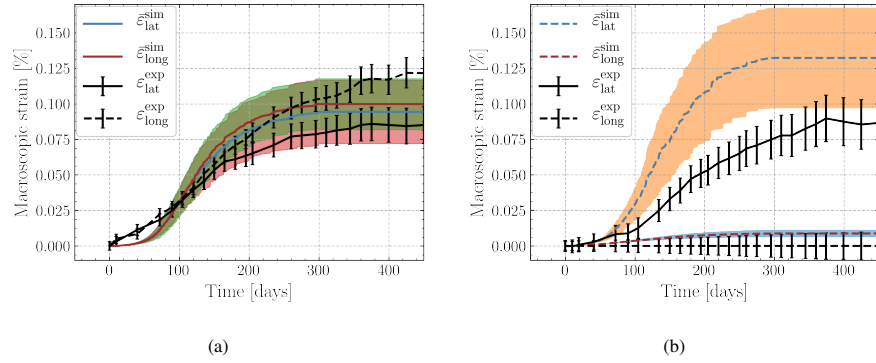


Figure 5: Macroscopic strain of numerical concrete specimens affected by ASR under (a) free-expansion conditions, (b) uniaxial compression loading of 10 MPa compared to the experimental results by Multon and Toutlemonde [2006]. [Presented by Gallyamov et al. [2020]].

to the opening of tens of microns, thus it would be difficult to distinguish these micro-cracks by a naked eye.

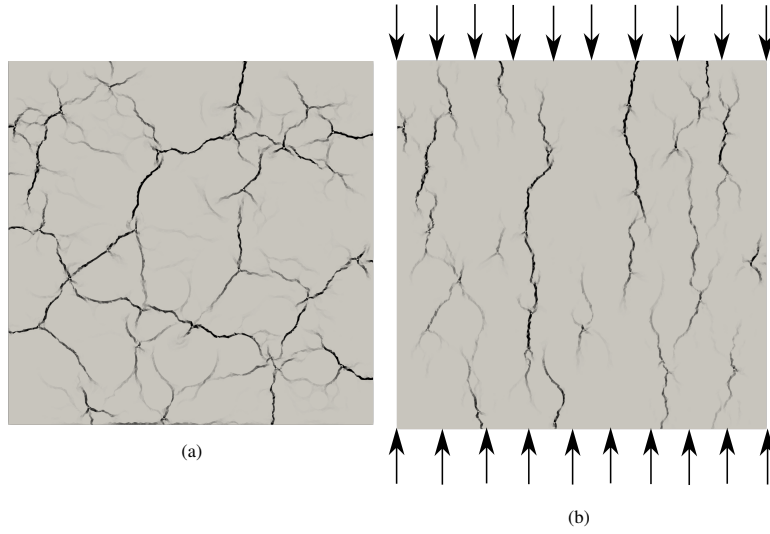


Figure 6: Crack opening maps of numerical concrete specimens affected by ASR under (a) free expansion conditions, (b) uniaxial compression loading of 10 MPa. [Presented by Gallyamov et al. [2020]].

### 3.2. Macro model

In this work a cross-section of the Salanfe gravity dam is chosen to study the mechanical behaviour of an ASR-affected dam and the role of temperature on it. Salanfe dam owned by Alpiq Suisse SA is located near Martigny (Valais), in Switzerland, and was built in 1952. Irreversible upstream deformations have been reported for the first



time in the early 1970's. In 2001, petrographic and SEM analysis finally proved that the dam is affected by ASR. Slot cutting, as a rehabilitation measure, was carried out on the dam in 2012 [Droz et al., 2013].

A cross-section in the middle of a long straight segment of the dam was chosen as the reference to minimise the 3D effect. Actual drawings of the dam as well as the field measurements of displacements, temperature and reservoir level were provided by the dam owner.

The 2D finite-element mesh of the cross-section is shown in Fig. 7 and consists of 250 triangular finite elements. Each finite element at the macro-scale (3 m size,

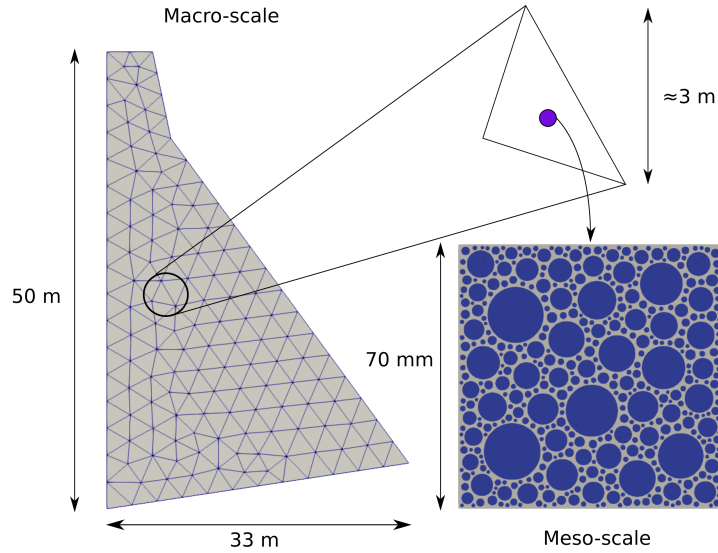


Figure 7: Macroscopic finite-element mesh of the cross-section of the dam and underlying concrete RVE.

on average) is linked to a single underlying RVE ( $70 \times 70 \text{ mm}^2$ ), which represents the heterogeneous structure of concrete at the meso-scale. The total number of RVEs corresponds to the number of finite elements in the macroscopic FE mesh because each macroscopic finite element contains only one integration point. The total number of degrees of freedom in the  $\text{FE}^2$  analysis is about 25,000,000 and the simulation was run on 280 processors.

The real foundation shape of the reference cross-section has a rough profile due



to the rock topology. The latter changes significantly from one joint to another. For simplification, the numerical model has a planar inclined foundation resembling the actual shape. To allow for certain relative movement of the dam bottom with respect to the underlying rock, a layer of interface finite elements was placed in-between. Its shear stiffness could be adjusted to modify the rigidity of the connection. For the basic case, its value was set to 4 MPa. The effect of the shear stiffness on the overall dam behaviour will be discussed further in the text.

The mechanical boundary conditions at the macro-scale are shown in Fig. 8. Two types of loads are acting on the dam: the load of the water and the load due to the self-weight. One component of the water load is applied along the upstream face with the hydrostatic distribution starting from the reservoir level down to the bottom. The second component acts upon the dam bottom as the hydrostatic uplift. Field data on water pressure under the dam was not available, thus the following pressure profile was suggested: pressure linearly drops from the reservoir bottom pressure to its third at the grout curtain position ( $\approx 5$  m from the upstream face in the downstream direction); later it linearly reduces to zero pressure at the downstream side.

The water level in the reservoir is not constant within a year. It is at its maximum in the winter months and at its minimum in summer. The intermittent real measurements of the water level were approximated by the continuous periodic parabolic curve shown in Fig. 9.

The boundary conditions for the heat transfer problem are illustrated in Fig. 10. They consist of either prescribing temperature at the model's contour (Dirichlet type) or temperature gradient (Neumann type). Actual record of air temperature in surroundings of Salanfe dam was used to establish its continuous sinusoidal approximation (see Fig. 11). Temperature applied at the concrete surface comprises the effect of air temperature and solar radiation. It is known that exposure to the sunlight can increase the temperature of structures significantly. Such increase, computed based on the building code SP 20.13330.2016 (in Russian), for the specific dam location and its orientation equals  $7.9^{\circ}\text{C}$  added on top of the daily mean temperature during the warm season. The above-mentioned code suggests same total solar radiation for vertical surfaces facing



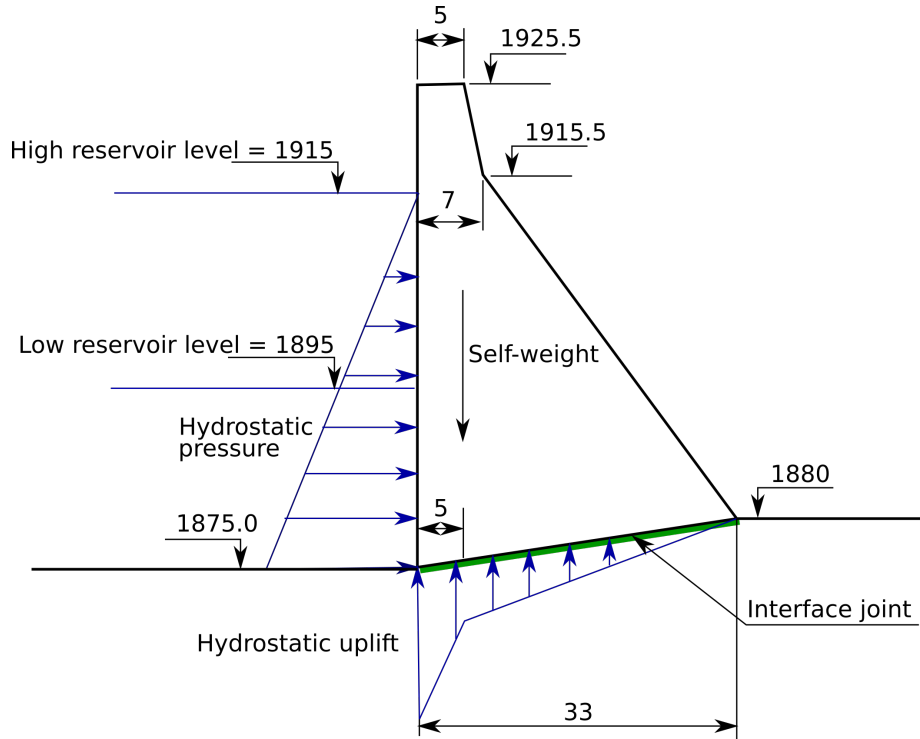


Figure 8: Altitudes and dimensions of the dam in meters and mechanical boundary conditions for the 2D model of the Salanfe dam.

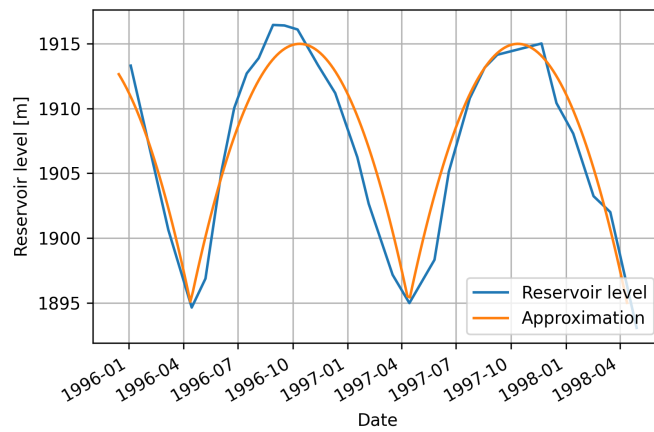


Figure 9: Real reservoir level fluctuations within two consequent years and its numerical approximation.



West or East. Although the lower part of the downstream face is inclined and thus attracts more solar radiation, we do not take this additional increment into account for simplicity. According to the meteorological reports, total annual sunshine in Western Switzerland is about 50%. To account for this information, annual surface temperature curve was build based on the air temperature curve by shifting the highest temperature value by the radiation increase and keeping the low value similar to the original one. To evaluate correctness of such approach, the proposed curve was integrated over 1 year and compared to an integral of a curve where half of a year had a constant increase of radiation contribution and the other half was equal to the air temperature. Final difference between two integrals was less than one % which proves the applicability of the proposed adjustment. Temperature of top of the soil was assumed to be equal to the air

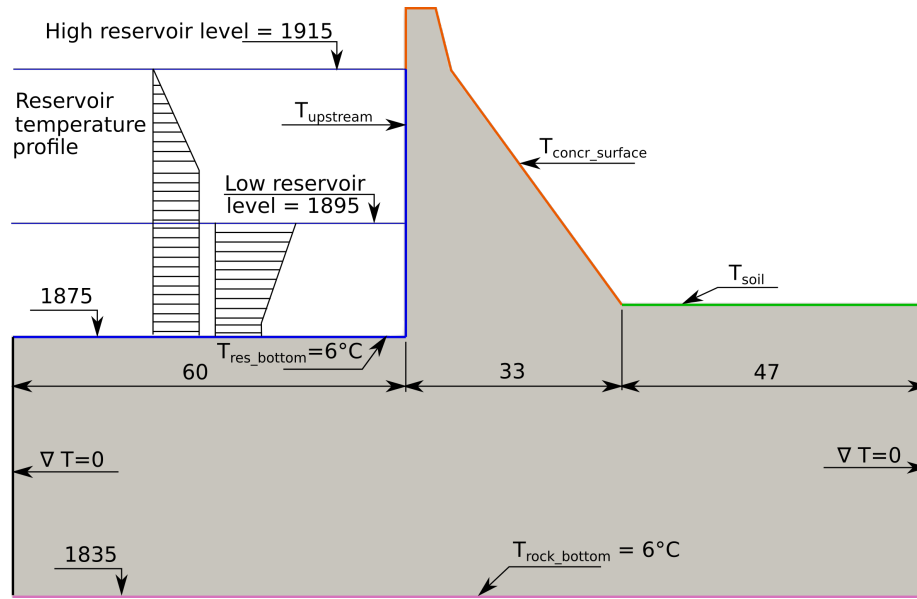


Figure 10: Boundary conditions for the macroscopic heat transfer problem.

temperature and radiation effect was discarded. Constant rock temperature of 6°C was assumed at the 40 m depth based on the data of Huang and Pietruszczak [1999] . Left and right borders of the rock mass were assigned homogeneous Neumann boundary condition ( $\nabla T = 0$ ). Water temperatures were taken from the field measurements of Vieux Emosson dam situated in the Salanfe's neighbouring valley. Temperature at the top is fluctuating between 10°C and 0°C. Fluctuations penetrate down to 15 m depth,



after which a constant temperature of  $6^{\circ}$  is applied and maintained down to the bottom of the reservoir.

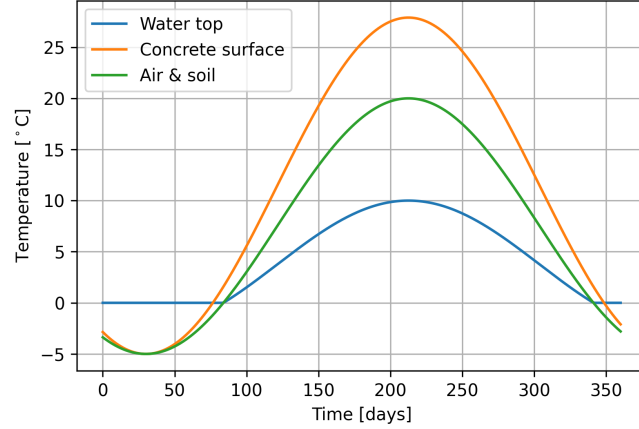


Figure 11: Approximations for the temperature fluctuations of air, top of the soil, concrete surface and top of the reservoir within a year.

## 4. Results

### 4.1. Field measurements

Performed numerical simulations were compared with the field data provided by the dam owner. This data includes horizontal displacements in the upstream-downstream (U-D) and left-right (L-R) directions as well as vertical (Z) movement of the crest. Horizontal displacements are available both at the level of the crest and at the base which are measured by direct and inverted pendulums correspondingly. Available data is shown in Fig. 12. Since the numerical model is two-dimensional, left-right displacement of the crest is ignored. The rest of the data is used for the comparison. Upstream-downstream movement of the crest has the longest historical track beginning right after the dam construction in 1953. The rest of the data (crest Z and base U-D movements) start its record in 1993. While the base movements are almost zero, the crest has substantial uplift. As there are no available data during preceding 40 years, the Z curve does not provide the absolute values of displacement, but rather the uplift rate. The image reveals that in the field conditions, expansion continues for already 68 years and



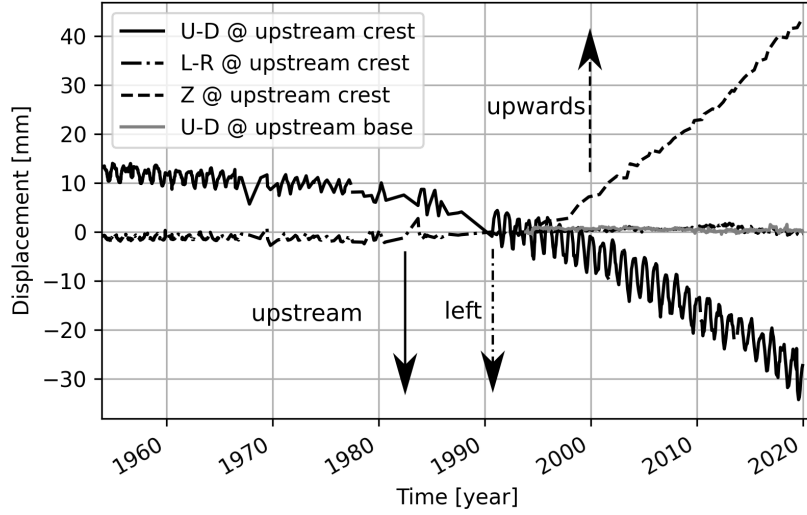


Figure 12: Field measurements of Salanfe displacements in the reference cross-section. U-D stands for the upstream-downstream direction, L-R for the left-right direction, and Z for the vertical direction.

it still goes on. In the subsequent figures, the initial offset of 13 mm was subtracted from the whole U-D curve as being not ASR-related. If the frequency of horizontal displacement varies between 1 to 4 measurements per month, the vertical displacement data is much more scarce and is measured 2 to 3 times per year.

Extra to the displacement measurements, the dam owner performs yearly inspections. One of the outcomes is an updated crack map of the surface. The latter is not presented here due to privacy. Authors could resume that in the block of interest, almost all the observed cracks are concentrated in the upper half of the upstream face with very most of them following the axis of the dam (horizontal lines on the upstream face). The latter makes the approach of 2D modelling of a cross-section valid: all the numerical cracks in a 2D model take form of infinite planes propagating along the dam axis when extrapolated to 3D.

History of measurement of the dam displacements, level of the reservoir and the temperature variation are provided in supplementary materials.



#### 4.2. ASR parameters

Simulation of the dam behaviour with the parameters of expansion law in Table 3, calibrated on the accelerated laboratory experiments, results in premature dam expansion and uplift halt within the first ten years after construction which does not correspond to the field observations (see Fig. A.21 of Appendix). In order to match the numerical results with field data, parameters of the ASR expansion law had to be recalibrated. The updated set of parameters is given in Table 4. Energy constant  $U_C$  got eliminated by making characteristic time  $\tau_{ch}$  in Eq. (7) independent of temperature and equal to the reference value  $\tau_{ch}(T_0)$ , and the reference temperature was reduced to 0°C. The actual values of the latency and characteristic times are not unique: both lower and higher values could have been chosen. The main purpose of taking such large numbers is to make the expansion linear within the studied time period. The minimum values of  $\tau_{lat}$  and  $\tau_{ch}$  for which the expansion curve stays linear are of order of 43 years.

Ratio of the ASR sites area to the aggregates area	0.1 %
Asymptotic strain $\varepsilon(\infty)$	37 %
Latency time $\tau_{lat}$	120.5 years
Characteristic time $\tau_{ch}$	123.29 years
Reference temperature $T_0$	0°C
Energy constant $U_C$	-
Energy constant $U_L$	400 K

Table 4: Updated parameters of the ASR-expansion law.

Comparison of the numerical outcome with the field data is plotted in Fig. 13. Displacements of the crest are measured for the top upstream point. Numerical results have a good agreement both with the vertical movement and the upstream drift of the crest. Similar to the field data, numerical horizontal drift curves have yearly fluctuations caused by the reservoir level change. While the rate of the simulated horizontal drift is matching the measured one perfectly, its vertical counterpart is by 25% slower than the field rate. This difference could possibly be explained by the 3D effect, which



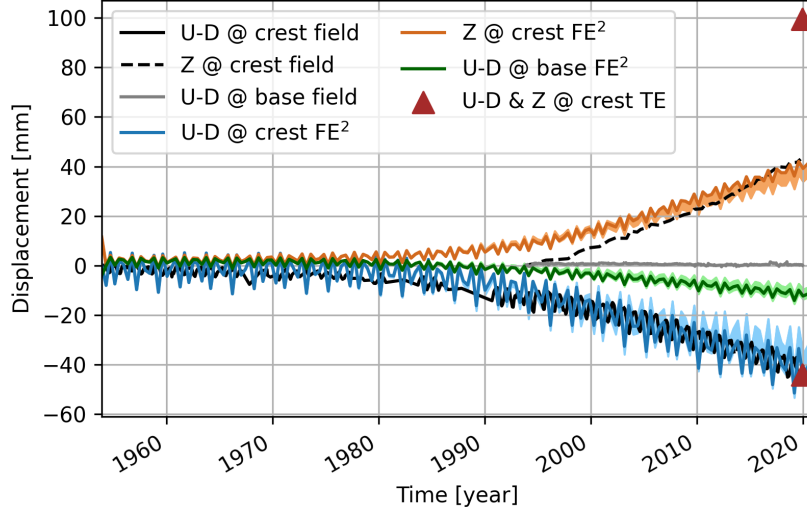


Figure 13: Comparison of the field measurements of the dam movement with the numerical results. Shaded areas represent variation between three simulations with different RVEs. TE stands for the isotropic thermo-elastic simulation.

is not captured by the model. High out-of-plane stress might play a role on the ASR-related expansion by hindering it in the dam-axis direction and boosting it in the other two. The horizontal drift of the upstream bottom point is not exactly zero as measurements indicate. The behaviour of the foundation is dictated by the shear stiffness of the interface between concrete and rock which will be demonstrated further in the text.

The macroscopic results depend on a specific RVE micro-structure and positions of the ASR-sites. To obtain a better statistical representation, two additional  $FE^2$  simulation with different positions of gel sites and distributions of tensile strength  $f_t$  within RVEs were conducted. The range of displacements between three simulations could be consulted in Fig. 13. As there is no significant variation between them, the results of the first simulation will be used further in the text.

For a better statistics, an ensemble of multi-scale simulations with different RVE micro-structures should be run. The result of this Monte Carlo simulation is a family of displacement curves forming a statistical distribution. The mean curve should match the field measurements. Otherwise, the expansion law parameters have to be adjusted



and the statistics updated. Described procedure is extremely computationally expensive and could not be performed within the scope of the current study. Based on the simulations with three different micro-structures and their deviations, we do not expect qualitatively different results from the ones presented above.

The final set of the expansion law parameters substantially differs from the ones based on the laboratory experiments. Employment of a less reactive concrete with lower alkali content could cause an increase in the  $\tau_{lat}$  and  $\tau_{ch}$ . However, this argument does not seem to be legit for their thousandth increase. Construction data does not have any track of ASR-mitigating additives used in Salanfe dam. The energy constant  $U_L$  was reduced significantly compared to the one identified by Ulm et al. [2000]. More than that,  $U_C$  had to be fully eliminated. Overall, the newly identified parameters made the thermal law less sensitive to the temperature variation and narrowed the gap between expansion rates of the coldest and the warmest parts of the dam. Moreover, the macroscopic expansion curve became linear, and expansion does not show signs of slowing down.

To obtain similar results, there is no need in the asymptotic expansion law, Eq. (7). Instead, a linear Arrhenius-inspired law could be formulated as follows:

$$\frac{\partial \varepsilon_{eig}(t, T)}{\partial t} = k e^{-(E_a/RT)}, \quad (19)$$

where  $k$  is some pre-exponential constant,  $E_a$  is the ASR activation energy,  $R$  is the universal gas constant and  $T$  is the temperature.  $E_a$  has double functionality: it defines the expansion rate as well as the sensitivity to the temperature difference.  $k$  is a scaling factor for the final curve. Ratio between expansion values for two constant temperatures and arbitrary time equals

$$\frac{\varepsilon_{eig}(T_1)}{\varepsilon_{eig}(T_2)} = e^{\frac{E_a}{R} \left( \frac{1}{T_2} - \frac{1}{T_1} \right)}. \quad (20)$$

Taking a zero limit of  $E_a$  would result in the exponential taking value of 1, which means equality between  $\varepsilon_{eig}(T_1)$  and  $\varepsilon_{eig}(T_2)$ . Oppositely, an increase in  $E_a$  would separate the two values. Previously,  $E_a$  for ASR was identified in a wide range of 10 – 50 kJ/mole



[Larive, 1997, Ben Haha, 2006, Mukhopadhyay et al., 2006, Ghanem et al., 2010].

To match the field data, the following parameters of the expansion law in Eq. (19) were used: pre-exponential constant  $k = 9.3\text{e-}6$  and activation energy  $E_a = 3$  kJ/mole. Results obtained with Eq. (7) and Eq. (19) match each other perfectly. Displacement curves obtained with Arrhenius equation are plotted in Fig. A.22 of Appendix. Similar to the previous case, the energy constant had to be reduced by more than ten times. Although the low value of  $E_a$  generally suggests high reactivity of aggregates, the reason for reducing  $E_a$  in our model was to minimise the difference in expansion values within the operational temperature range. To counteract the increase in expansion due to the reduction of  $E_a$ , a small value of  $k$  had to be adopted. An equilibrium between values of  $E_a$  and  $k$  allowed us to keep the expansion rate low and close to the measurements.

Identified mismatch between the laboratory and field-based parameters suggests that there is a certain gap between two conditions. The issue of predicting field behaviour based on the accelerated tests was repeatedly discussed in the literature (i.e. Ideker et al. [2012a,b], Fournier et al. [2009], Durand and Fournier [2016]). Expansion results obtained within accelerated mortar bar test at 80°C (AMBT), concrete prism test at 38°C (CPT) and exposure field sites for the same concrete are not monotonous [Ideker et al., 2012b]. ? pointed at progressive loss of correlation between concrete prism expansion under 38°C and relative humidity > 95% and the 15-year expansions in concrete blocks stored outdoors. A recent study by ? proved that accelerated tests are useful for determining the reactivity of aggregates, however correlation of expansion magnitude between laboratory experiments and field exposure sites is complicated.

We realize that there is a substantial difference in the model calibration parameters. The laboratory temperature range at which expansion law was calibrated does not cover the field conditions, and this results in a change in environmental conditions. Most of the accelerated ASR tests are done at temperatures above 20°C [Ulm et al., 2000, Larive, 1997, Ben Haha, 2006, Gautam and Panesar, 2016, Multon and Toutlemonde, 2006] which is above the upper limit of the current field range in Switzerland. It is possible that ASR experiments at accelerated temperatures result in different physics and chemistry than what happens in field conditions. Other factors that also could



have contributed to the identified difference are that laboratory concrete experiences significant alkali leaching [Lindgård et al., 2018], which does not take place in massive concrete in field conditions; the relative humidity of a dam differs from the assumed full saturation conditions: reduced RH would slow ASR down and to test this hypothesis field data on concrete humidity at different positions of a dam would be required; we do not model alkalis transport and ASR-products migration within cracks and pores.

#### 4.3. Temperature effect

With the calibration completed, we focus next on the ASR effects within the dam structure. Gel strain  $\varepsilon_{ig}$  accumulated at the end of simulation is shown in Fig. 14a. There is a slight increase of the gel strain from the upstream underwater part towards

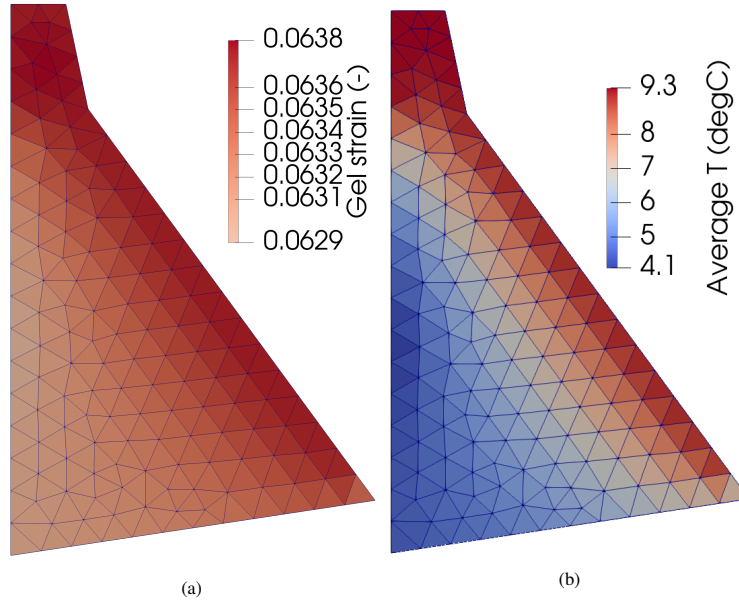


Figure 14: a) Accumulated gel strain at the end of the last time step. b) Macroscopic temperature averaged over the simulation time.

downstream and the crest. This gradient is caused by the upstream having in average lower temperature during the year than the downstream. The lowest gel strain values are concentrated in the middle upstream zone, as temperatures there could take values between 0 and 6°C in winter. The two extreme gel strain values differ insignificantly (0.062 and 0.063 for the minimum and the maximum values).



To have a clear understanding on the contribution of this gel strain difference to the overall dam displacement an additional multi-scale simulation was performed. The latter comprised no heat flow simulation, but only a mechanical FE<sup>2</sup> model with a constant temperature applied across the entire dam. The temperature value was obtained by spatial and temporal averaging within the dam cross-section and was equal to 8°C. The parameters of the ASR-expansion law were kept the same. All the displacement curves are exactly matching the results of the thermo-mechanical multi-scale simulation. Corresponding curves could be consulted in Fig. A.23 of Appendix. This study proves that the homogeneous gel strain results in the same deformation profile of the dam as in the non-homogeneous case with small gel strain variation. Therefore, the numerical model demonstrated that within the specific environmental conditions (specific temperature range, dam geometry and reservoir fluctuations), temperature difference has a negligible effect on the ASR evolution within the structure.

Macroscopic temperature averaged over the simulation time is presented in Fig. 14b. Gel strain accumulation for minimum and maximum average temperatures, which are 4.1°C and 9.3°C correspondingly, is plotted in Fig. 15. These curves were obtained from Eq. (7) by applying constant temperature values and the parameters from Table 4. One can observe that the original curves have a very small gap in-between which illustrates low sensitivity to the temperature variation within considered temperature window. To understand how higher sensitivity (therefore higher energy constants) would affect model behaviour, two additional simulations were performed. Parameters of the expansion law were modified to have larger expansion difference between cold and warm areas. This resulted in constant temperature curves plotted in Fig. 15 (by stars and circles). First set of parameters ( $\tau_{lat} = 41.1$  year,  $\tau_{ch} = 230$  year,  $U_L = 4500$  K) produces the same gel strain for low temperature and higher strain for 9.3° C. Second set ( $\tau_{lat} = 41.1$  year,  $\tau_{ch} = 298.6$  year,  $U_L = 4500$  K) has an opposite effect. In physical terms, the first set would increase gel expansion in the warmer part compared to the simulation presented below, while the second set would reduce expansion in the cold part. The rest of the parameters were kept unchanged with respect to Table 4. Multi-scale simulations were performed with these two sets of parameters. The results are



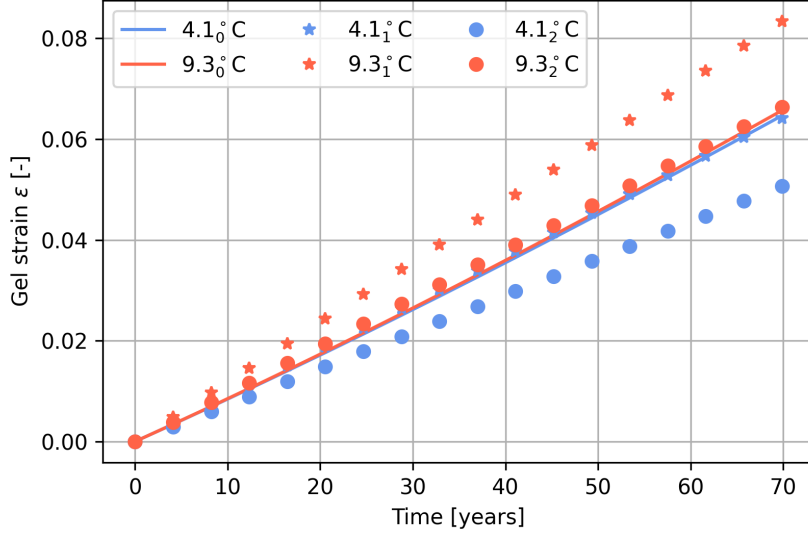


Figure 15: Gel strain evolution for two extreme temperatures for original parameters of the expansion law (solid line) and two sets of curves for modified parameters.

plotted in Fig. 16. The first set of parameters, as expected, results in premature U-D and Z crest displacements because of the “warm” area accumulating higher gel strain values. The results of the second set are somehow intriguing: although the “cold” area is producing less gel strain, U-D displacement of the crest still starts earlier and goes above the field measurements. This is happening because of the difference in the gel strain values of the “warm” and “cold” zones: the “warm” area will produce an additional “push” of the crest in the upstream direction due to the expansion advantage over the “cold” one, independently of the absolute values. Contrary to the case with different expansion values, having the same expansion across the entire cross section minimises the U-D drift and brings it close to the observations.

Oppositely to the horizontal displacements, expansion magnitude is directly linked to the vertical crest displacement: higher gel strains across the dam cause higher crest uplift. These two additional simulations demonstrate that the model does not have to be sensitive to the temperature variations within the considered temperature gap in order to match available field measurements. The constant expansion across the dam has to be high enough to cause the sufficient uplift.



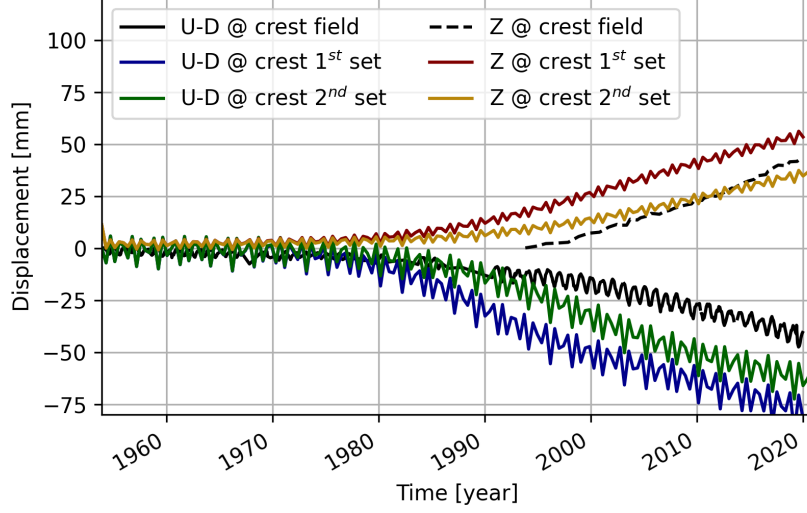


Figure 16: Crest displacements for 2 sets of the expansion law parameters compared to the field data. Base displacements are omitted for brevity.

#### 4.4. Expansion anisotropy

It is of great importance to state that the homogeneous gel strain distribution does not cause homogeneous expansion within the cross-section. So called ASR-expansion anisotropy manifests itself in the form of loading-dependent expansion. Current numerical model successfully reproduces ASR-anisotropy which was demonstrated in [Gallyamov et al., 2020]. To highlight the ASR-anisotropy effect in the dam simulation, we compare the multi-scale results to the thermo-elastic simulation with no damage. In the latter, expansion is caused by applying homogeneous hydrostatic eigenstrain  $\varepsilon_{eig}$  across the dam cross-section (similar to the thermo-elastic expansion). The eigenstrain value is chosen in a way to match the horizontal crest drift. Final vertical and horizontal displacement values are plotted in Fig. 13 by triangles. The elastic crest uplift is by 140% higher than the multi-scale one. Such difference owes to the expansion anisotropy present in the  $FE^2$  simulation and emphasises the need for including the anisotropic effect into ASR models.

Comparison of the full thermo-mechanical multi-scale model with its homogeneous-temperature modification have shown that the difference in gel strain is not sufficient



to cause the horizontal drift. However, there are two other causes of the latter:

- orthogonal triangle shape of the dam;
- different levels of expansion anisotropy at the upstream and downstream dam faces.

The geometrical component could be identified directly from the thermo-elastic simulation (see Fig. 13). Having the same expansion values of the vertical upstream and inclined downstream faces, the latter is longer which produces greater length increase. This difference in extensions makes the whole structure extend upwards and bend upstream (see Fig. 17c). Following this logic, a dam having an isosceles triangle shape would have only vertical uplift due to the homogeneous ASR extent.

The second contributor to the horizontal drift is the non-homogeneous expansion anisotropy across the dam cut. This is illustrated in Fig. 17a. Black segments here denote principal strains at integration points. Their directions correspond to the principal directions. Sizes of segments were obtained by multiplying the actual principal strain values by some scaling factor to make them visible. Principal strains and their directions were computed by the eigenvalue analysis of the small strain tensor  $\epsilon$  in Eq. (6). Although there is certain rotation taking place, its contribution to the deformation gradient is negligible. This eliminates the need to compute more complex deformation measures (such as right or left Cauchy-Green tensors) and allows to operate the simple strain  $\epsilon$ . All values of principal strain are positive. The maximum extension corresponding to the maximum segment size is 0.12%.

Coloured background denotes the ratio between two principal strain values. While the warm shades indicate an expansion state close to isotropic, the cool ones denote areas with orthotropic expansion. The downstream wall and the crest are primarily expanding isotropically as they are not constrained nor heavily loaded. The foundation is restrained by the underlying rock, thus its horizontal movement is limited, which minimises its horizontal strain. The red area in the right bottom corner has the most isotropic state. It could be explained by the transition between the restrained lower boundary and the free downstream side. The most interesting observation on this plot



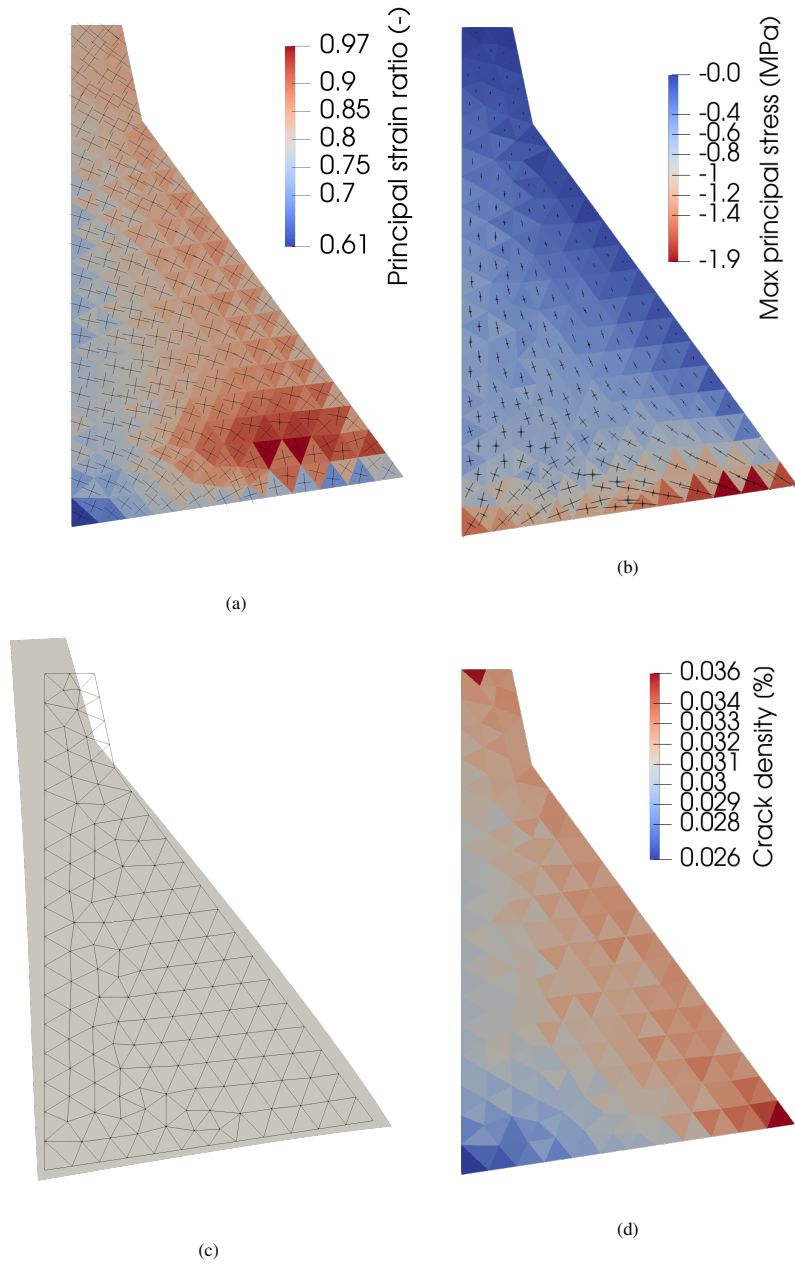


Figure 17: a) Ratio between the principal strains in colour. Segments denote direction and amplitude of principal strains at each integration point. b) Coloured background represents crack density. Principal stresses are denoted by segments. c) Deformed shape of the dam in comparison with the initial configuration (amplification factor of 100). d) Crack density map quantifying the ratio between the total crack opening area and the RVE area.



is the slightly blue area on the upstream side of the dam. In this zone, principal strain directions are close to horizontal and vertical. The horizontal strain is 1.3 times larger than the vertical one. The reason for this could be deduced from Fig. 17b where the principal stresses are plotted. Colours here denote amplitudes of the highest principle stress. The load coming from the self-weight and the reservoir pressure generates compressive stresses which transition from being nearly vertical in the upper part to almost horizontal at the base. Such transition is due to two factors: the presence of the horizontal load of the reservoir pressure which has to be transmitted to the underlying rock; and the horizontal constraint at the bottom which gives rise to high compressive stresses in response to the concrete's expansion. The highest principal stresses pass through the area next to the upstream wall and impose compressive forces on the corresponding RVEs. Although the stress values are relatively small ( $\approx 0.4 - 1.0$  MPa), it is sufficient to partially hinder the vertical ASR expansion.

To further illustrate the loading effect, crack density map in Fig. 17d and crack opening maps in Fig. 18 are given. Crack density map is visualising the ratio between

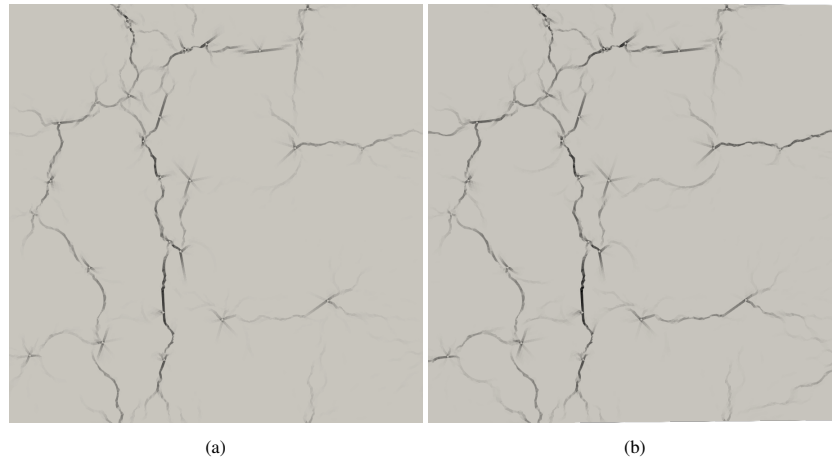


Figure 18: Crack opening maps of the RVEs on the a) upstream and b) downstream sides at the age of 42 years.

the total crack area and the area of an RVE. Indeed, RVEs on the upstream side have slightly lower area of cracks in comparison to the downstream side. Two typical RVEs on the upstream and downstream sides at the age of 42 years are plotted in Fig. 18. The reason for choosing this intermediate step is the possibility to clearly distinguish the



difference between two patterns, while at the end of the simulation it becomes complicated due to the abundance of cracks. The intensity of grey here denotes the crack opening. The darkest shade corresponds to an opening of  $40\text{ }\mu\text{m}$ . Such crack is difficult to distinguish by visual inspection. The downstream RVE has more horizontally oriented cracks. Moreover, horizontal cracks present in both RVEs are wider open in the downstream RVE. Since expansion in our model comes mainly from propagation and opening of cracks, two typical crack maps explain why the expansion is orthotropic on the upstream side and close to isotropic on the downstream one. Expansion is never exactly isotropic due to its dependence on a specific RVE micro-structure and gel positions.

While simulation results show variation of crack density from the upstream face to the downstream, the field observations show more developed cracking in the upper part of both faces. A possible explanation for such discrepancy could be the 3D effect not captured by the model.

#### 4.5. *The concrete-rock interface*

The effect of the interface between the dam and the rock below was investigated by modifying its shear stiffness. If in the original simulation its value was 4 MPa which allowed for substantial sliding, here it was increased to 4 GPa bringing it into the range of rock-like materials. For a better match in the upstream-downstream direction of the crest, the latency time  $\tau_{lat}$  had to be reduced to 109.6 years.

While the crest displacements were not significantly affected by this change, the horizontal drift at the base was almost eliminated, which brings it even closer to the field data. Therefore, the stiffness of the concrete-rock interface is controlling the foundation horizontal displacement. Results of this simulation are plotted in Fig. A.24 of Appendix.

More consequences of the stiff interface could be observed in Fig. 19. Due to the rigidity of the dam foundation, the horizontal expansion is constrained and the principal strain ratio reduces down to the 0.2 – 0.3 range. Two bottom corners show negative strain ratio due to the highest stress concentrations. Reduced horizontal expansion



comes at the cost of high compressive stresses shown in Fig. 19b. The range of the principal stress values along the foundation is 3 – 10 MPa, which is few times higher than the stresses caused by the self-weight of the structure ( Fig. 17b). Two RVEs,

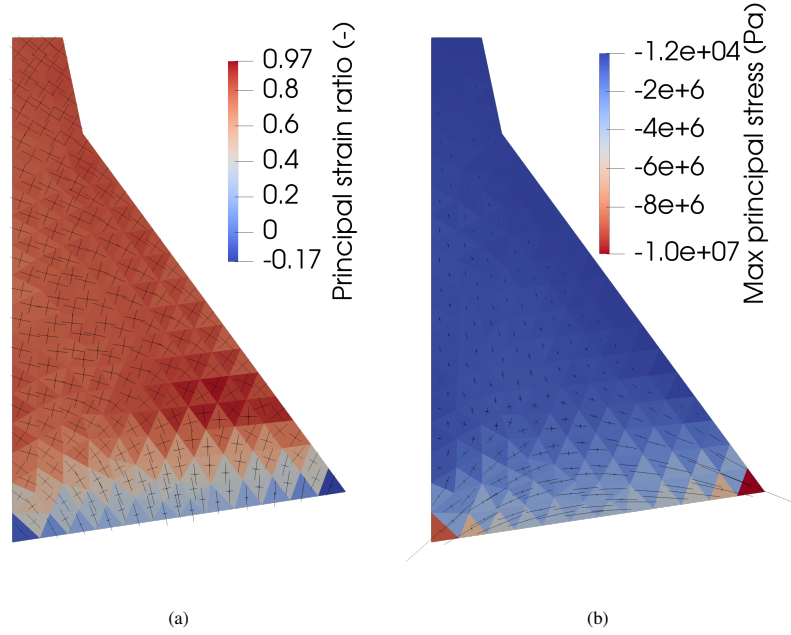


Figure 19: a) Principal strains (segments) and ratio between them (colour) for the stiff concrete-rock interface simulation. b) Compressive principal stresses for the same simulation.

one from the bottom and one from the crest, are compared at the end of the simulation in Fig. 20. Crack in the bottom RVE are predominantly horizontal while the crest ones have random orientations. This horizontal cracks alignment is due to the strong uniaxial compression setting the preferable crack orientation.

Important to discuss here that the high compressive stresses in the foundation are partially caused by the idealistic elastic behaviour of the underlying rock. The latter develops tensile stress in response to the expansion of the foundation. Thus, compression in the foundation is equilibrated by the tension in the rock. In reality, the underlying rock is far from being a continuous elastic material: it has pre-existing fissures and also can fracture. The full tensile strain applied to the rock will be partially accumulated by the rock mass movement, while the rest of it will contribute to the stress evolution. Additionally, the tensile strength of the rock is also imposing a cap on the maximum



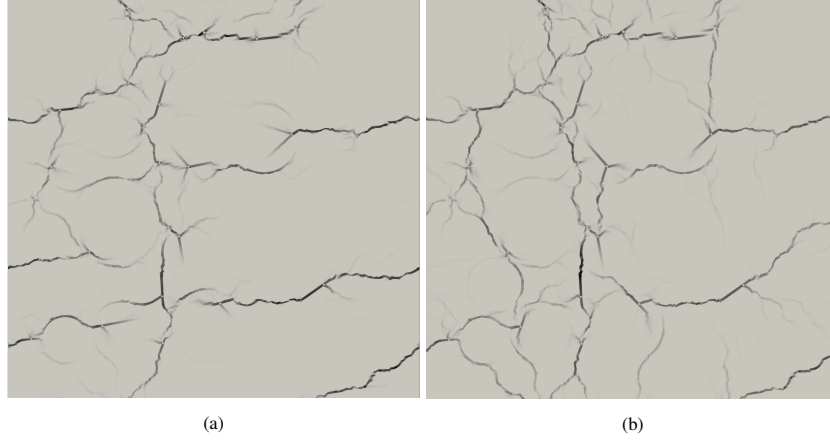


Figure 20: Crack opening maps of the RVEs at the a) bottom and the b) crest at the age of 70 years.

possible tensile stress in the rock. For most of the rock types used as foundations, its value is in 5 – 14 MPa range [Demirdag et al., 2019]. Therefore, our model gives an upper limit estimate for the stresses in the foundation. Better prediction could be obtained by using more sophisticated rock model, e.g. Hoek-Brown model. More field data on the underlying rock is necessary (GSI, RMR, tensile strength and stiffness).

## 5. Conclusions

In the current work, a 2D thermo-mechanical multi-scale model of concrete deterioration by ASR was presented. After reviewing the principles of the method, the model was applied to simulate the behaviour of the ASR-affected Salanfe dam in Western Switzerland. The model was calibrated to match the field measurements. Obtained set of parameters and constants of the ASR expansion law substantially differs from the parameters matching the accelerated laboratory experiments on ASR expansion of concrete. As the possible reason for the gap between two sets of parameters, could be different dynamics of ASR (both in chemistry and physics) happening in the low temperature range compared to the accelerated laboratory tests. Moreover, the expansion saturation, commonly seen in laboratory experiments, could not be observed in the field data where expansion is predominantly linear. This fact also suggests that there is a gap between the laboratory conditions and field. While temperature variation can significantly alter expansion rate of concrete in laboratory conditions, its role on ASR



advancement in a dam is negligible according to the model.

Structural analysis of the dam revealed some interesting insights. The upstream drift and vertical uplift at the level of the dam's crest were attributed to the difference in length between the upstream and the downstream faces rather than different ASR-strains within a structure. Having the same level of expansion, the longer downstream face pushes the crest in the upstream direction.

Although ASR is advanced to the same level within the whole cross-section, concrete strain is only partially isotropic. The most of isotropic expansion is happening along the downstream face, while the bottom upstream part has more pronounced horizontal expansion. Such behaviour was attributed to the sensitivity of ASR-expansion to the external load: the self-weight of the structure partially hindered evolution of horizontal cracks in corresponding RVEs reducing vertical ASR-expansion. Another area with anisotropic ASR expansion is the dam's foundation. Vertical strains there prevail over horizontal ones due to the restraining effect of the rock below. Given a competent rock, such expansion constraint could lead to evolution of compressive stresses few times larger than the ones coming from the self-weight.

## **Acknowledgments**

The Swiss National Science Foundation is acknowledged for financial support within the Sinergia project "Alkali-silica reaction in concrete (ASR)" through grant CRSII5\_17108. The authors would also like to thank Olivier Vallotton (Stucky SA) for fruitful discussions.



## References

- M. Alnaggar, G. Di Luzio, and G. Cusatis. Modeling Time-Dependent Behavior of Concrete Affected by Alkali Silica Reaction in Variable Environmental Conditions. Materials, 10(5):471, Apr. 2017. ISSN 1996-1944. doi: 10.3390/ma10050471. URL <http://www.mdpi.com/1996-1944/10/5/471>.
- N. A. Aniskin and A. M. Shaytanov. Assessment of Temperature Effect on the Stress-Strain Behavior of a Concrete Gravity Dam. Power Technol Eng, 54(2):154–159, July 2020. ISSN 1570-145X, 1570-1468. doi: 10.1007/s10749-020-01183-1. URL <http://link.springer.com/10.1007/s10749-020-01183-1>.
- F. Bangert, D. Kuhl, and G. Meschke. Chemo-hygro-mechanical modelling and numerical simulation of concrete deterioration caused by alkali-silica reaction. Int. J. Numer. Anal. Meth. Geomech., 28(78):689–714, June 2004. ISSN 0363-9061, 1096-9853. doi: 10.1002/nag.375. URL <http://doi.wiley.com/10.1002/nag.375>.
- Z. P. Bažant and B. H. Oh. Crack band theory for fracture of concrete. Matériaux et Construction, 16:155–177, 1983.
- M. Ben Haha. Mechanical effects of alkali silica reaction in concrete studied by sem-image analysis. PhD thesis, EPFL, Lausanne, Switzerland, 2006.
- A. F. Bower. Applied Mechanics of Solids. CRC Press, 0 edition, Oct. 2009. ISBN 978-1-4398-0248-9. doi: 10.1201/9781439802489. URL <https://www.taylorfrancis.com/books/9781439802489>.
- R. Charlwood and I. Sims. A Review of the Effectiveness of Strategies to Manage Expansive Chemical Reactions in Dams and Hydro Projects. In Swelling Concr. Dams Hydraul. Struct., pages 3–39, 2017.
- E. Coenen, V. Kouznetsova, and M. Geers. Novel boundary conditions for strain localization analyses in microstructural volume elements: BCS FOR LOCALIZATION ANALYSIS IN MICROSTRUCTURES. Int. J. Numer. Meth. Engng, 90



- (1):1–21, Apr. 2012. ISSN 00295981. doi: 10.1002/nme.3298. URL <http://doi.wiley.com/10.1002/nme.3298>.
- C. Comi, R. Fedele, and U. Perego. A chemo-thermo-damage model for the analysis of concrete dams affected by alkali-silica reaction. *Mechanics of Materials*, 41(3): 210–230, Mar. 2009. ISSN 01676636. doi: 10.1016/j.mechmat.2008.10.010. URL <https://linkinghub.elsevier.com/retrieve/pii/S0167663608001464>.
- C. Comi, B. Kirchmayr, and R. Pignatelli. Two-phase damage modeling of concrete affected by alkali-silica reaction under variable temperature and humidity conditions. *International Journal of Solids and Structures*, 49(23-24):3367–3380, Nov. 2012. ISSN 00207683. doi: 10.1016/j.ijsolstr.2012.07.015. URL <https://linkinghub.elsevier.com/retrieve/pii/S0020768312003009>.
- A. I. Cuba Ramos, C. Roux-Langlois, C. F. Dunant, M. Corrado, and J.-F. Molinari. HPC simulations of alkali-silica reaction-induced damage: Influence of alkali-silica gel properties. *Cement and Concrete Research*, 109:90–102, July 2018. ISSN 00088846. doi: 10.1016/j.cemconres.2018.03.020. URL <https://linkinghub.elsevier.com/retrieve/pii/S000888461731150X>.
- M. J. DeJong, M. A. Hendriks, and J. G. Rots. Sequentially linear analysis of fracture under non-proportional loading. *Engineering Fracture Mechanics*, 75(18):5042–5056, Dec. 2008. ISSN 00137944. doi: 10.1016/j.engfracmech.2008.07.003. URL <https://linkinghub.elsevier.com/retrieve/pii/S0013794408002099>.
- S. Demirdag, K. Tufekci, N. Sengun, T. Efe, and R. Altindag. Determination of the Direct Tensile Strength of Granite Rock by Using a New Dumbbell Shape and its Relationship with Brazilian Tensile Strength. *IOP Conf. Ser.: Earth Environ. Sci.*, 221:012094, Mar. 2019. ISSN 1755-1315. doi: 10.1088/1755-1315/221/1/012094. URL <https://doi.org/10.1088/1755-1315/221/1/012094>. Publisher: IOP Publishing.
- P. Droz, O. Vallotton, T. Menouillard, and R. Leroy. Slot cutting an AAR-affected dam: case study of the Salanfe dam. *Hydropower and Dams*, page 4, 2013.



- C. F. Dunant and K. L. Scrivener. Micro-mechanical modelling of alkali-silica-reaction-induced degradation using the AMIE framework. Cement and Concrete Research, 40(4):517–525, Apr. 2010. ISSN 00088846. doi: 10.1016/j.cemconres.2009.07.024. URL <https://linkinghub.elsevier.com/retrieve/pii/S0008884609001847>.
- C. F. Dunant and K. L. Scrivener. Effects of aggregate size on alkali-silica-reaction induced expansion. Cement and Concrete Research, 42(6):745–751, June 2012a. ISSN 00088846. doi: 10.1016/j.cemconres.2012.02.012. URL <https://linkinghub.elsevier.com/retrieve/pii/S0008884612000403>.
- C. F. Dunant and K. L. Scrivener. Effects of uniaxial stress on alkali-silica reaction induced expansion of concrete. Cement and Concrete Research, 42(3):567–576, Mar. 2012b. ISSN 00088846. doi: 10.1016/j.cemconres.2011.12.004. URL <https://linkinghub.elsevier.com/retrieve/pii/S0008884611003267>.
- B. Durand and B. Fournier. 20-year results of an in-situ monitoring study of large concrete electrical tower foundations affected by alkali-silica reaction (ASR). In ICAAR 15 Proceedings, page 10, July 2016.
- R. Esposito and M. A. N. Hendriks. Literature review of modelling approaches for ASR in concrete: a new perspective. European Journal of Environmental and Civil Engineering, 23(11):1311–1331, Nov. 2019. ISSN 1964-8189, 2116-7214. doi: 10.1080/19648189.2017.1347068. URL <https://www.tandfonline.com/doi/full/10.1080/19648189.2017.1347068>.
- F. Feyel and J.-L. Chaboche. FE2 multiscale approach for modelling the elastoviscoplastic behaviour of long fibre SiC/Ti composite materials. Computer Methods in Applied Mechanics and Engineering, 183(3-4):309–330, Mar. 2000. ISSN 00457825. doi: 10.1016/S0045-7825(99)00224-8. URL <https://linkinghub.elsevier.com/retrieve/pii/S0045782599002248>.
- B. Fournier, J. H. Ideker, K. J. Folliard, M. D. Thomas, P.-C. Nkinamubanzi, and R. Chevrier. Effect of environmental conditions on expansion in concrete due



- to alkali-silica reaction (ASR). Materials Characterization, 60(7):669–679, July 2009. ISSN 10445803. doi: 10.1016/j.matchar.2008.12.018. URL <https://linkinghub.elsevier.com/retrieve/pii/S1044580308003513>.
- E. Gallyamov, A. Cuba Ramos, M. Corrado, R. Rezakhani, and J.-F. Molinari. Multi-scale modelling of concrete structures affected by alkali-silica reaction: Coupling the mesoscopic damage evolution and the macroscopic concrete deterioration. Int J Solids Struct, 207:262–278, Dec. 2020. ISSN 00207683. doi: 10.1016/j.ijsolstr.2020.10.010. URL <https://linkinghub.elsevier.com/retrieve/pii/S0020768320303942>.
- B. P. Gautam and D. K. Panesar. A new method of applying long-term multi-axial stresses in concrete specimens undergoing ASR, and their triaxial expansions. Mater Struct, 49(9):3495–3508, Sept. 2016. ISSN 1359-5997, 1871-6873. doi: 10.1617/s11527-015-0734-z. URL <http://link.springer.com/10.1617/s11527-015-0734-z>.
- H. Ghanem, D. Zollinger, and R. Lytton. Predicting ASR aggregate reactivity in terms of its activation energy. Construction and Building Materials, 24(7):1101–1108, July 2010. ISSN 0950-0618. doi: 10.1016/j.conbuildmat.2009.12.033. URL <https://www.sciencedirect.com/science/article/pii/S0950061809004449>.
- V. Gocevski and E. Yildiz. Numerical Analysis of AAR Affected Structures with Slot-Cuts. In Swelling Concr. Dams Hydraul. Struct., pages 263–276, 2017.
- R. M. Gunn, K. L. Scrivener, and A. Leemann. The Identification, Extent and Prognosis of Alkali-Aggregate Reaction Related to Existing Dams in Switzerland. In Swelling Concr. Dams Hydraul. Struct., pages 117–143, 2017.
- A. Hilaire, A. B. Giorla, C. F. Dunant, L. Sofia, and K. L. Scrivener. Behavior of Concrete Deteriorated by ASR under Triaxial Load. In Swelling Concr. Dams Hydraul. Struct., pages 55–74, 2017.
- R. Hill. Elastic properties of reinforced solids: Some theoretical principles. Journal of the Mechanics and Physics of Solids, 11(5):357–372, Sept. 1963. ISSN 00225096.



- doi: 10.1016/0022-5096(63)90036-X. URL <https://linkinghub.elsevier.com/retrieve/pii/002250966390036X>.
- M. Huang and S. Pietruszczak. Modeling of Thermomechanical Effects of Alkali-Silica Reaction. Journal of Engineering Mechanics, 125(4):476–485, Apr. 1999. ISSN 0733-9399, 1943-7889. doi: 10.1061/(ASCE)0733-9399(1999)125:4(476).
- J. H. Ideker, T. Drimalas, A. Bentivegna, K. J. Folliard, B. Fournier, M. D. Thomas, R. D. Hooton, and C. Rogers. The importance of outdoor exposure site testing. In ICAAR 12 Proceedings, Austin, Texas, USA, 2012a.
- J. H. Ideker, K. J. Folliard, M. Juenger, and A. Bentivegna. Do Current Laboratory Test Methods Accurately Predict Alkali-Silica Reactivity? MJ, 109(4), 2012b. ISSN 0889-325X. doi: 10.14359/51683914. URL <http://www.concrete.org/Publications/ACIMaterialsJournal/ACIJJournalSearch.aspx?m=details&ID=51683914>.
- T. Iskhakov, J. J. Timothy, and G. Meschke. Expansion and deterioration of concrete due to ASR: Micromechanical modeling and analysis. Cement and Concrete Research, 115:507–518, Jan. 2019. ISSN 00088846. doi: 10.1016/j.cemconres.2018.08.001. URL <https://linkinghub.elsevier.com/retrieve/pii/S0008884618301509>.
- V. Kouznetsova, W. A. M. Brekelmans, and F. P. T. Baaijens. An approach to micro-macro modeling of heterogeneous materials. Computational Mechanics, 27(1):37–48, Jan. 2001. ISSN 0178-7675, 1432-0924. doi: 10.1007/s004660000212. URL <http://link.springer.com/10.1007/s004660000212>.
- C. Larive. Apports combinés de l’expérimentation et de la modélisation à la compréhension de l’alcali-réaction et de ses effets mécaniques. PhD thesis, l’École Nationale des Ponts et Chaussées, 1997.
- A. Leemann and P. Lura. E-modulus of the alkali-silica-reaction product determined by micro-indentation. Construction and Building Materials, 44:221–227,



- July 2013. ISSN 09500618. doi: 10.1016/j.conbuildmat.2013.03.018. URL <https://linkinghub.elsevier.com/retrieve/pii/S0950061813002237>.
- A. Leemann and B. Münch. The addition of caesium to concrete with alkali-silica reaction: Implications on product identification and recognition of the reaction sequence. *Cement and Concrete Research*, 120:27–35, June 2019. ISSN 00088846. doi: 10.1016/j.cemconres.2019.03.016. URL <https://linkinghub.elsevier.com/retrieve/pii/S0008884619300730>.
- A. Leemann, T. Katayama, I. Fernandes, and M. A. T. M. Broekmans. Types of alkali–aggregate reactions and the products formed. *Proceedings of the Institution of Civil Engineers - Construction Materials*, 169(3):128–135, June 2016. ISSN 1747-650X, 1747-6518. doi: 10.1680/jcoma.15.00059. URL <http://www.icevirtuallibrary.com/doi/10.1680/jcoma.15.00059>.
- J. Lindgård, T. Østnor, B. Fournier, Ø. Lindgård, T. Danner, G. Plusquellec, and K. De Weerd. Determining alkali leaching during accelerated ASR performance testing and in field exposed cubes using cold water extraction (CWE) and XRF. *MATEC Web Conf.*, 199:03004, 2018. ISSN 2261-236X. doi: 10.1051/mateconf/201819903004. URL <https://www.matec-conferences.org/10.1051/mateconf/201819903004>.
- T. Menouillard, J.-F. Seignol, L.-I. Boldea, P. Roure, A. Tzenkov, and R. M. Gunn. A model of concrete swelling for describing the Kariba dam. Valencia, Spain, 2011.
- C. Miehe, J. Schröder, and J. Schotte. Computational homogenization analysis in finite plasticity Simulation of texture development in polycrystalline materials. *Computer Methods in Applied Mechanics and Engineering*, 171(3-4):387–418, Apr. 1999. ISSN 00457825. doi: 10.1016/S0045-7825(98)00218-7. URL <https://linkinghub.elsevier.com/retrieve/pii/S0045782598002187>.
- Ministry. SP 20.13330.2016 [in Russian]. Technical report, Ministry of Construction and Housing and Communal Services of the Russian Federation, 2016.



- T. Miura, S. Multon, and Y. Kawabata. Influence of the distribution of expansive sites in aggregates on microscopic damage caused by alkali-silica reaction: Insights into the mechanical origin of expansion. Cement and Concrete Research, 142:106355, Apr. 2021. ISSN 0008-8846. doi: 10.1016/j.cemconres.2021.106355. URL <https://www.sciencedirect.com/science/article/pii/S0008884621000041>.
- A. K. Mukhopadhyay, C.-S. Shon, and D. G. Zollinger. Activation Energy of Alkali-Silica Reaction and Dilatometer Method. Transportation Research Record, 1979(1):1–11, Jan. 2006. ISSN 0361-1981, 2169-4052. doi: 10.1177/0361198106197900102. URL <http://journals.sagepub.com/doi/10.1177/0361198106197900102>.
- S. Multon and A. Sellier. Multi-scale analysis of alkali-silica reaction (ASR): Impact of alkali leaching on scale effects affecting expansion tests. Cement and Concrete Research, 81:122–133, Mar. 2016. ISSN 00088846. doi: 10.1016/j.cemconres.2015.12.007. URL <https://linkinghub.elsevier.com/retrieve/pii/S0008884615300168>.
- S. Multon and F. Toutlemonde. Effect of applied stresses on alkali-silica reaction-induced expansions. Cement and Concrete Research, 36(5):912–920, May 2006. ISSN 00088846. doi: 10.1016/j.cemconres.2005.11.012. URL <https://linkinghub.elsevier.com/retrieve/pii/S0008884605002838>.
- W. Puatatsananon and V. Saouma. Chemo-Mechanical Micromodel for Alkali-Silica Reaction. ACI Materials Journal, page 12, 2013.
- J. Renard. Etude de l’initiation de l’endommagement dans la matrice d’un matériau composite par une méthode d’homogenisation. Aerosp. Sci. Technol., 6:37–51, 1987.
- E. Robertson. Thermal properties of rock. Open-File Report 88-441, United States Department of the Interior Geological Survey, 1988. Series: Open-File Report.
- J. G. Rots. Sequentially linear continuum model for concrete fracture. Fracture Mechanics of Concrete Structures, page 9, 2001.



- J. G. Rots and J. Blaauwendraad. Crack models for concrete: discrete or smeared? Fixed, Multi-directional or rotating? HERON, 34(1), 1989.
- J. G. Rots and S. Invernizzi. Regularized sequentially linear saw-tooth softening model. Int. J. Numer. Anal. Meth. Geomech., 28(78):821–856, June 2004. ISSN 0363-9061, 1096-9853. doi: 10.1002/nag.371. URL <http://doi.wiley.com/10.1002/nag.371>.
- SCD. Concrete swelling of dams in Switzerland. Report of the Swiss Committee on Dams on the state of concrete swelling in Swiss Dams, Swiss Committee on Dams, 2017.
- P. M. Suquet. Introduction. In: Sanchez-Palencia E., Zaoui A. (eds) Homogenization Techniques for Composite Media. Lecture Notes in Physics. In E. Sanchez-Palencia and A. Zaoui, editors, Homogenization Techniques for Composite Media, volume 272, pages 193–198. Springer Berlin Heidelberg, Berlin, Heidelberg, 1987. ISBN 978-3-540-17616-9 978-3-540-47720-4. doi: 10.1007/3-540-17616-0\_15. URL [http://link.springer.com/10.1007/3-540-17616-0\\_15](http://link.springer.com/10.1007/3-540-17616-0_15). Series Title: Lecture Notes in Physics.
- R. N. Swamy. Alkali-silica reaction in concrete. Blackie and Son ; Taylor and Francis e-Library, Glasgow, England; New York, New York, 2003. ISBN 978-0-203-20033-9. URL <https://www.taylorfrancis.com/books/0203036638>. OCLC: 1132080496.
- F.-J. Ulm, O. Coussy, L. Kefei, and C. Larive. Thermo-Chemo-Mechanics of ASR Expansion in Concrete Structures. J. Eng. Mech., 126(3):233–242, Mar. 2000. ISSN 0733-9399, 1943-7889. doi: 10.1061/(ASCE)0733-9399(2000)126:3(233).
- S. Xu and Y. Zhu. Experimental determination of fracture parameters for crack propagation in hardening cement paste and mortar. Int J Fract, 157(1-2):33–43, May 2009. ISSN 0376-9429, 1573-2673. doi: 10.1007/s10704-009-9315-x. URL <http://link.springer.com/10.1007/s10704-009-9315-x>.



## Appendix A. Displacement plots

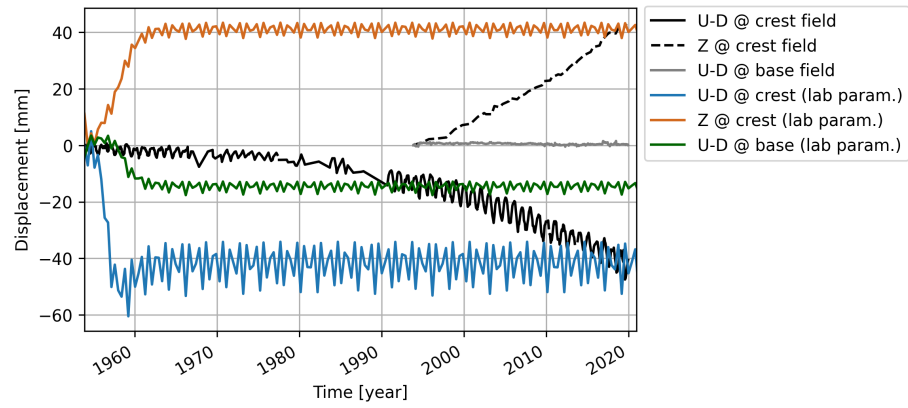


Figure A.21: Displacements at the crest and the bottom of the dam obtained by employing the expansion law parameters calibrated on the accelerated laboratory experiments. Comparison to the field measurements shows a mismatch.



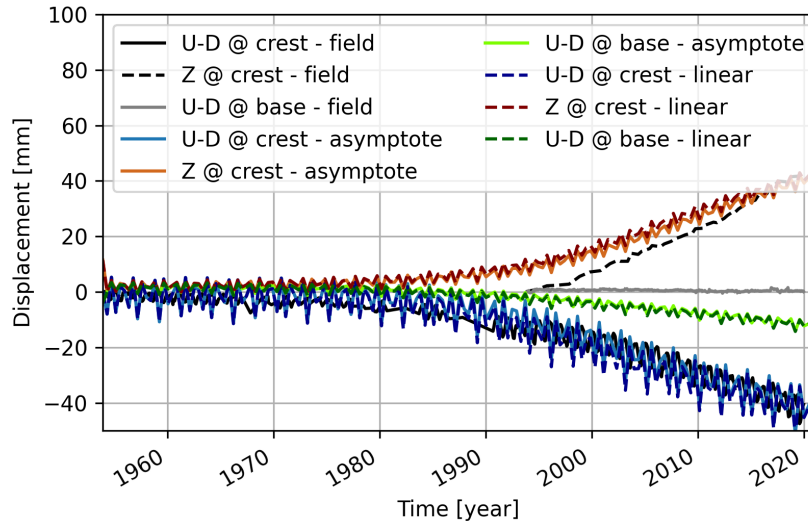


Figure A.22: Comparison between the results obtained by the asymptotic expansion law from Eq. (7) and the linear one from Eq. (19).

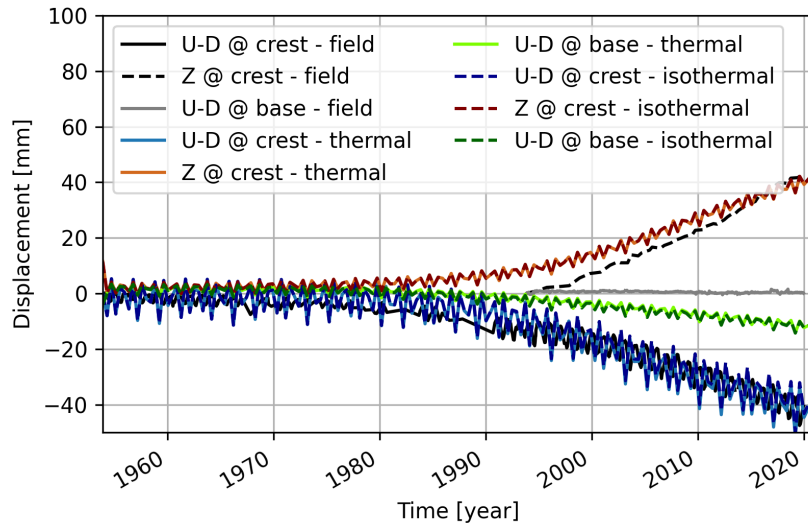


Figure A.23: Results of the isothermal simulation with average temperature applied across the dam compared to the full thermo-mechanical model and field measurements.



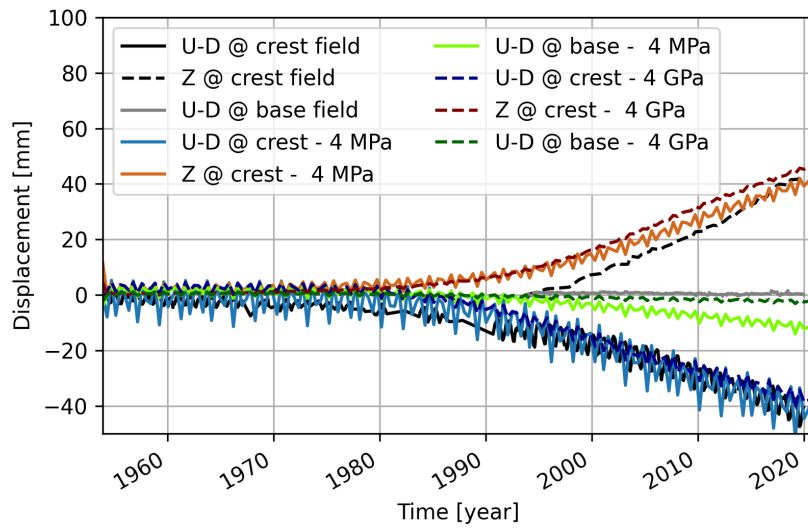


Figure A.24: Crest and bottom displacements of the dam with two different shear stiffness values of the concrete-rock interface.